Nuclear Lamins A/C and B1 Provide a Structural Framework That Organizes and Anchors Nuclear Pore Complexes

Mark Kittisopikul[1,2†], **Takeshi Shimi**[1,3†‡], **Meltem Tatli**[4], **Joseph R. Tran**[5], **Yixian Zheng**[5], **Ohad Medalia**[4], **Khuloud Jaqaman**[2,6], **Stephen A. Adam**[1], **Robert D. Goldman**[1]

***For correspondence:** r-goldman@northwestern.edu (RDG)

[†]These authors contributed equally to this work

Present address: [‡] IIR Advanced Research Center for Cell Biology, Tokyo Institute of Technology, Yokohama, Kanagawa, Japan 226-8503

[1]Department of Cell and Developmental Biology, Feinberg School of Medicine, Northwestern University, Chicago, IL; [2]Department of Biophysics, UT Southwestern Medical Center, Dallas, TX; [3]Cell Biology Center and World Research Hub Initiative, Institute of Innovative Research, Tokyo Institute of Technology, Yokohama, Japan; [4]Department of Biochemistry, University of Zurich, Zurich, Switzerland; [5]Department of Embryology, Carnegie Institution for Science, Baltimore, MD; [6]Lyda Hill Department of Bioinformatics, UT Southwestern Medical Center, Dallas, TX

Abstract Nuclear lamin isoforms assemble into fibrous meshworks within the nuclear lamina (NL) where they are associated with nuclear pore complexes (NPCs). Although the lamins and NPCs are major components of the nuclear envelope (NE), little is known about their structural relationships. We used 3D structured illumination microscopy (3D-SIM) and sub-pixel image analysis to show that NPCs are closely associated with lamin fibers in mouse embryonic fibroblasts (MEFs). When lamin A/C (LA/C) or lamin B1 (LB1) are removed by gene knockout, the NPCs retained their association and redistributed with the resulting enlarged lamin meshworks. Cryo-ET revealed that more LA/C than LB1 fibers contacted the nucleoplasmic ring of NPCs. Knockdown of the outer ring nucleoporin ELYS induced NPC clusters that excluded LA/C fibers. Knockdown of the basket nucleoporin TPR reduced the size of LA/C, LB1, and LB2 meshworks while retaining their close association with NPCs. NUP153 knockdown reduced LA/C and B2 meshwork size in wild type (WT) MEFs and caused NPC clustering in nuclei lacking LB1. Therefore, lamins and nucleoporins act together to maintain the organization and distribution of lamin meshworks and NPCs.

Introduction

Two major components of the nuclear envelope (NE) are the type V intermediate filament proteins, the nuclear lamins, and nuclear pore complexes (NPCs) (***Aebi et al., 1986***; ***Fisher et al., 1986***; ***Goldman et al., 1986***; ***McKeon et al., 1986***). The four lamin isoforms LA, LC, LB1, and LB2 are mainly associated with the inner nuclear membrane where they assemble into discrete meshworks of fibers composing the nuclear lamina (NL). The NPCs penetrate the NE forming transport passageways delineated by the fusion of the inner and outer nuclear membranes, thereby allowing for bidirectional transport across the NE. They are composed of multiple copies of 30 proteins known

as nucleoporins (**Beck and Hurt, 2016**). Both the nuclear lamins and NPC structures are closely associated with chromatin at the nuclear periphery (**Guelen et al., 2008**; **Peric-Hupkes et al., 2010**; **Ibarra and Hetzer, 2015**).

The lamins are classified as A-type (LA, LC) and B-type (LB1, LB2). LA and LC are derived from the *Lmna* gene by alternative splicing (**Lin and Worman, 1993**), whereas LB1 and LB2 are encoded by *Lmnb1* and *Lmnb2*, respectively (**Höger et al., 1990**; **Biamonti et al., 1992**; **Lin and Worman, 1995**; **Maeno et al., 1995**). Lamins assemble into a 13.5 nm thick layer composed of 3.5 nm diameter filaments underlying the inner nuclear membrane in mouse embryo fibroblast (MEF) nuclei (**Turgay et al., 2017**). Using three-dimensional structured illumination microscopy (3D-SIM) combined with computer vision analysis, we demonstrated that these lamin filaments, termed fibers in the light microscope, are non-randomly organized into complex interwoven meshworks within the NL (**Shimi et al., 2015**; **Turgay et al., 2017**). Notably, each lamin isoform appears to assemble into a distinct meshwork, each with a similar structural organization (**Shimi et al., 2015**). However, the meshworks formed by individual lamin isoform fibers are significantly expanded in size in *Lmna* or *Lmnb1* knockout (KO) MEF nuclei compared to the lamin meshworks in WT or *Lmnb2* KO MEF nuclei demonstrating that LA/C and LB1 interactions are required for normal lamin fiber meshwork structure in WT MEFs (**Shimi et al., 2015**).

For many years, it has been apparent that there are structural interactions between the NL and the NPCs of eukaryotic nuclei. The earliest studies on identification of components of the NE identified a cell free NPC-NL fraction that could be isolated under fairly stringent conditions suggesting a strong physical association between these major NE components (**Kay et al., 1972**; **Dwyer and Blobel, 1976**; **Scheer et al., 1976**; **Aebi et al., 1986**). In addition, both lamins and the NPCs are relatively immobile in the plane of the NE indicating that both are anchored in some fashion (**Broers et al., 1999**; **Moir et al., 2000**; **Rabut et al., 2004**). Thin section electron microscopy studies of the NE have shown that the NPCs are located in spaces where both the lamina and heterochromatin appear to be discontinuous (**Fawcett, 1966**; **Ou et al., 2017**). Our previous study by cryo-ET also supports the close association of lamin filaments with the NPCs (**Turgay et al., 2017**; **Tatli and Medalia, 2018**) and biochemical results have shown interactions between lamins and a subset of specific nucleoporins (**Hase and Cordes, 2003**; **Krull et al., 2004**; **Al-Haboubi et al., 2011**). More recently, proximity-dependent biotin identification, BioID, recognized several lamin-associated nucleoporins including Nup153, ELYS and TPR (**Roux et al., 2012**; **Xie et al., 2016**). These nucleoporins localize to the nucleoplasmic aspect of NPCs which lie in close proximity to the NL (**Walther, 2001**; **Rasala et al., 2008**). The distribution of NPCs is nonrandom with characteristic center to center spacing varying according to species ranging from human to frog (**Maul, 1977**). Furthermore, removal of all lamins from mouse MEFs or mESC derived fibroblast-like cells leads to clustering of the NPCs, which can be rescued by re-expression of either A or B-type lamins (**Guo and Zheng, 2015**). These observations suggest that lamins play an important role in regulating the distribution of NPCs.

Although the extant evidence strongly suggests that lamins interact with nucleoporins to anchor the NPCs in the NE, the specific lamins involved in this anchorage remain unknown. In this study, we investigate the structural relationships between each lamin isoform fiber meshwork and NPCs at nanoscale precision using 3D-SIM with newly developed computational procedures for sub-pixel quantitative image analysis. This quantitative approach is necessitated by the complexity of the four lamin fiber meshworks and NPCs located within a thin layer at the nuclear surface. The results of our analyses demonstrate that NPCs are closely associated with lamin fibers. At higher resolution cryo-ET confirms that both LA/C and LB1 filaments interact closely with the NPCs at the nucleoplasmic ring. Targeted disruption of nucleoporins and lamin isoforms demonstrates the interdependence of the spatial distributions of lamin fibers and NPCs.

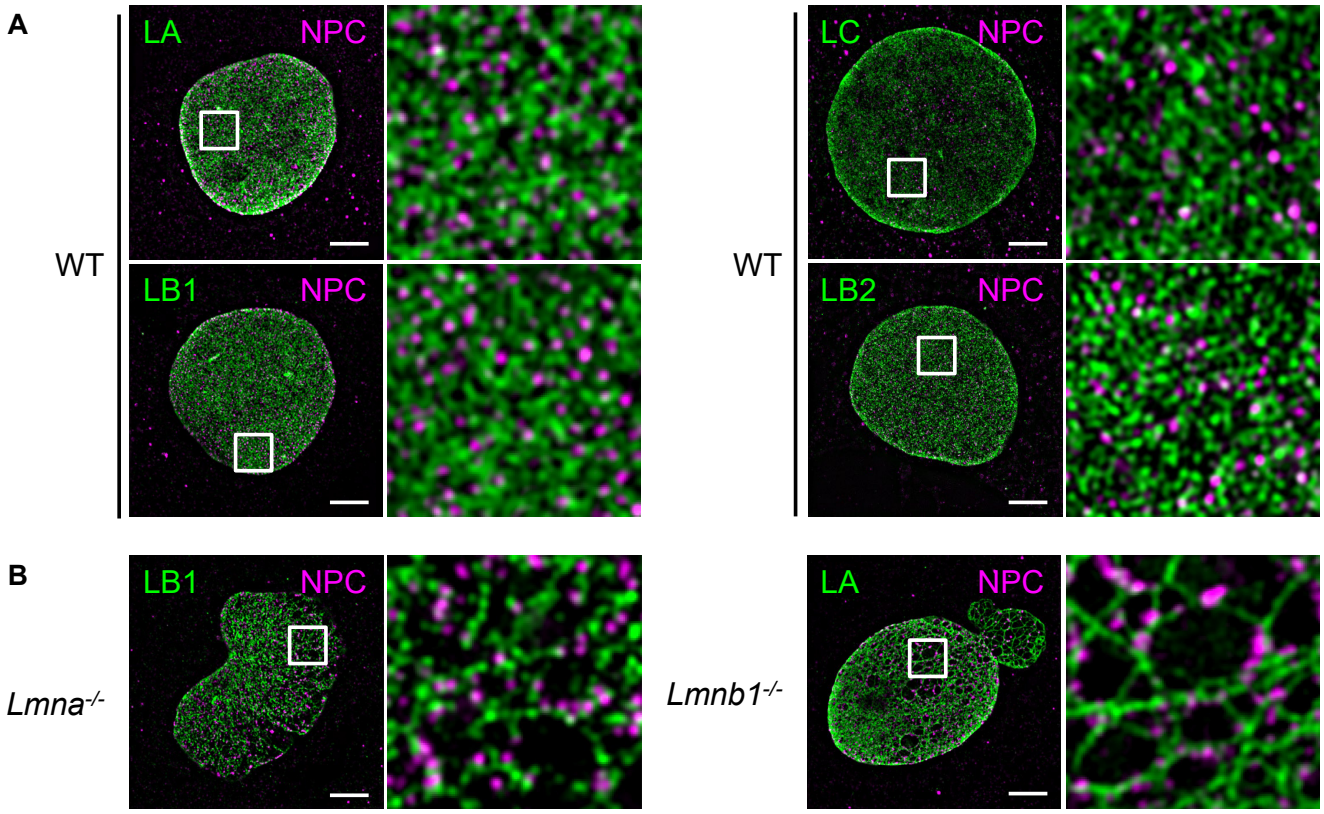

Figure 1. Co-Distribution of Lamin Fibers and NPCs. Colabeling of lamins and nuclear pore complexes in wt and lamin KO MEF nuclei using indirect immunofluorescence with a pair of specific antibodies against each lamin isoform (LA, LB1, LB2 or LC) and the FXFG-repeat nucleoporins. A) wt MEF nuclei colabeled with the indicated lamin isoform and FXFG-repeated nucleoporins. B) Nuclei of *Lmna*$^{-/-}$ (left pair) and *Lmnb1*$^{-/-}$ (right pair) MEFs. The indicated areas with white squares are enlarged approximately eight-fold along each edge and displayed on right side of each pair of images. Scale bar = 5 μm.

Results

NPCs are structurally linked to lamin fibers

We used 3D-SIM and image reconstruction to determine the structural relationships among immunolabeled lamin fiber meshworks and NPCs in MEFs. NPCs in WT MEFs were distributed all across the NL region, but did not show an obvious co-localization with any of the lamin meshworks, as indicated by the very few white areas in merged overlays (Figure 1A). This was remarkable because some co-localization of lamins and NPCs would be expected by chance given the densely packed environment of the NL. This lack of co-localization between lamins and NPCs suggested the existence of a bona fide spatial relationship. We took advantage of our previous finding that the spaces or "faces" delineated by lamin fibers comprising the meshworks increase in size in *Lmna*$^{-/-}$ and *Lmnb1*$^{-/-}$ MEF nuclei (***Shimi et al., 2015***). This allowed us to examine the association between NPCs and specific lamin isoforms in WT, *Lmna*$^{-/-}$, and *Lmnb1*$^{-/-}$ MEFs. Importantly, NPCs remained in close proximity to the LA and LB1 fibers in the expanded meshworks of *Lmna*$^{-/-}$ and *Lmnb1*$^{-/-}$ MEF nuclei and were absent in the meshwork faces (Figure 1B). These results strongly suggest that LA and LB1 are required for the normal distribution of NPCs. Although these images provide qualitative evidence that there is an association between lamin isoform fibers and NPCs, it is important to verify such associations using a quantitative approach to ascertain the extent of the relationships between each lamin fiber isoform and NPCs.

Image analysis reveals specific spatial relationships between lamin fibers and NPCs

We developed quantitative image analysis tools to precisely determine the spatial relationships between lamin isoform fibers and NPCs, and to localize both structures with sub-pixel precision in dense and sparse lamin meshworks (Figure 2A; details of analysis tools in Materials and Methods). We reasoned that by measuring the distances between the centers of lamin fibers and the center of lamin meshwork faces to the centers of NPCs (Figure 2 – Figure Supplement 1), we could quantitatively assess the association of NPCs with individual lamin isoforms. To evaluate the frequency of observing distances between the lamin fibers or face centers and NPCs by chance, we compared our observed distance measurements to the expected distances under a null hypothesis, which assumes the NPCs and lamin meshworks have no relationship and are thus independently distributed. For example, we measured the LA fiber center to NPC center distance in WT cells as compared to the expected distances assuming no relationship (Figure 2B compare the measured data in the blue violin plot on top vs the expected distances in the red violin plots on bottom). By examining the difference in the observed from the expected distributions (Figure 2C), we could see a paucity (green) or excess (purple) of NPCs at certain distances from the centers of LA fibers. For example, in a single WT nucleus we observed fewer NPCs within 30 nm of the fibers and an excess of NPCs between 30 and 100 nm relative to the null hypothesis (green area; Figure 2C WT). In order to validate this approach, we performed the same analysis of the LA fiber to NPC distance in a single *Lmnb1*$^{-/-}$ MEF nucleus (Figure 2B). As in the WT nucleus, we saw an excess of NPCs between 30 and 100 nm in the *Lmnb1*$^{-/-}$ nucleus (Figure 2C). This agreed with the qualitative observation that the NPCs were associated with, but not co-localized with lamin fibers (Figure 1A,B, 2A).

Measuring the distance from the lamin face centers to NPCs allowed us to more precisely determine how NPCs are related to the lamin fibers. The faces are delineated by the lamin fibers composing the lamin isoform meshwork (Figure 2A; ***Shimi et al.*** (***2015***)). Their centers are points that are locally the most distant from the lamin fibers. This analysis also allowed us to account for changes in face size such as the enlargement seen in *Lmnb1*$^{-/-}$ or *Lmna*$^{-/-}$ nuclei (Figures 1B, 2A). Measuring both the distances of the NPCs to the lamin fibers and the centers of the faces, allowed us to examine a 2D bivariate statistical distribution in a single nucleus (Figure2 – Figure Supplement 1). To explore if the NPCs also had a relationship with the center of the faces, we found the points the most distant from the lamin fibers within a local area (white Xs, Figure 2A). For a circle, this would be the center, but other shapes may have multiple centers (see Methods). We measured the distances between the center of the NPCs and the center(s) of the faces (Figure 2 - Figure Supplement 1 G) and then compared that distribution to the null hypothesis (Figure 2D, E). In both the WT and the *Lmnb1*$^{-/-}$ nucleus, we observed median distances that were smaller than expected. This means that the NPCs were closer to the center of the faces than expected by chance. This is consistent with the observation that NPCs did not directly colocalize with the lamin fibers, but had a lateral proximal relationship.

We combined the distances of the NPCs to the lamin fibers and the distances of the NPCs from the face centers into two-dimensional histograms to represent the bivariate distribution (Figure 2 - Figure Supplement 1). The two-dimensional histograms showed that there was an expectation that NPCs would be near the LA fibers and away from the faces by chance in a broad distribution. However, the NPCs were offset from the LA fibers in a narrower than expected distribution (Figure 2 - Figure Supplement 1A-F). In the WT MEFs, the negative correlation between the distances was also apparent, which is expected since the NPCs that are farther from the lamin fibers tend to be closer to the face centers (Figure 2 Supplement 1A, B). However, the two-dimensional histograms of single nuclei were sparse and noisy indicating that additional distance measurements were needed for evaluation.

The localizations of both lamin fibers and NPCs were based on finding local maxima within the continuous reconstruction of the fluorescence intensity from critically sampled 3D-SIM images and was not dependent on rounding to the nearest pixel (See Methods and Supplement; Kittisopikul et

al. BioRxiv 2019). Here we focused on localizing lamin fibers and NPCs resolved by 3D-SIM, and not their specific molecular components consisting of individual 3.5 nm lamin filaments ***Turgay et al. (2017)*** and/or specific nucleoporins. Furthermore, we measured the distance between structures localized within two channels separated by their chromatic properties, and thus these distance measurements were not limited by resolution (***Stelzer, 1998***). The main limitations to the precision of the localization and distance measurements are the inaccuracy of indirect immunofluorescence labeling, signal-to-noise ratio, and structured illumination microscopy reconstruction artifacts. This was mitigated by examining the distribution of tens of thousands of distance measurements. These analyses permitted us to express the magnitude of differences in the co-distributions, or the lack thereof, in terms of nanometers with high statistical power (see Appendix 1).

The association between lamin fibers and NPCs is isoform dependent

We previously found that the four main lamin isoforms (LA, LC, LB1, and LB2) form independent meshworks (***Shimi et al., 2015***), and we sought to see if each isoform had a distinct relationship with NPCs.

Having established our approach to analyzing lamin-NPC associations, we measured the distances between the center of individual NPCs and the center of the nearest lamin fiber across the surface closest to the coverslip of 10 WT nuclei for each lamin isoform. Overall, the data obtained supports the lack of direct colocalization between NPCs and lamin fibers, which we observed qualitatively and quantitatively in single nuclei (Figures 1, 2). The median distances from the centers of NPCs to the centers of LA fibers (40.4 nm; $p < 0.001$; Table 1A, Figure 3A, Figure 3 – Figure Supplement 1A) and to the centers of LB1 fibers (38.1 nm; $p < 0.001$; Table 1A, Figure 3A) were similar. The observed median distances were 6 nm greater than the expected distribution (+6.9 nm LA; +6.0 nm LB1; Table 1A, Figure 3A, B; Figure 3 – Figure Supplement 1C). The expected distribution represents the distances between NPCs and lamins that we would expect under the null hypothesis that there is no relationship between the position of NPCs and lamins. It was calculated by a Monte Carlo simulation randomly placing a NPC within the segmented area of the nucleus. The median distance between NPCs and the center of faces in the LA meshworks was similar (119.3 nm; -11.7 nm vs expected; $p < 0.001$; Table 1B) or LB1 (118.3 nm; -10.8 nm vs expected; $p < 0.001$; Table 1B) and both median distances were less than expected if the lamins and NPCs were not associated (Figure 3C; Table 1B). These data show that NPCs and LA or LB1 fibers are not directly colocalized, but have a proximal lateral relationship. These findings suggest that NPCs and LA or LB1 fibers are structurally linked within the NL.

In contrast to the relationships between the NPCs and LA or LB1, the median distance from LC fibers to NPC centers did not differ significantly from expected (32.8 nm observed, + 0.7 nm vs expected; $p= 0.37$; Table 1A, Figure 3A, Figure 3 – Figure Supplement 1B). Also, the standard deviation of distances between LC fibers and NPCs (35.0 nm observed, -14.5 nm vs expected; $p=0.01$; Table 1A, Figure 3A) was not significant when using a Bonferonni corrected alpha level. While the p-value of 0.01 is smaller than the traditional alpha level of 0.05, we conducted multiple comparisons and thus need to compensate for Type I error. The Bonferroni correction of the alpha level across the 12 pairs of distributions compared in Tables 1A and 1B leads to an alpha level of $0.05/12 \approx 0.004$. However, the median distance determined for the NPC center to LC face center differed from the expected distribution (122.4 nm observed, -3.3 nm vs expected; $p < 0.001$; Table 1B, Figure 3C). While these measurements followed a pattern similar to that detected for LA and LB1, the magnitude of the differences were much smaller for LC (Figure 3C, D, Table 1B). Overall, these data suggested that the offset between NPCs and LC fibers is closer (median: 32.8 nm) than between NPCs and LA or LB1 fibers (medians: 40 nm). However, given the small differences in the LC fiber to NPC center measurements relative to expected, we cannot completely reject the null hypothesis for the LC fiber to NPC distances.

The relationship between LB2 fibers and NPCs in WT MEFs differed from the other lamin isoforms. We observed a statistically significant difference in medians from expected distributions

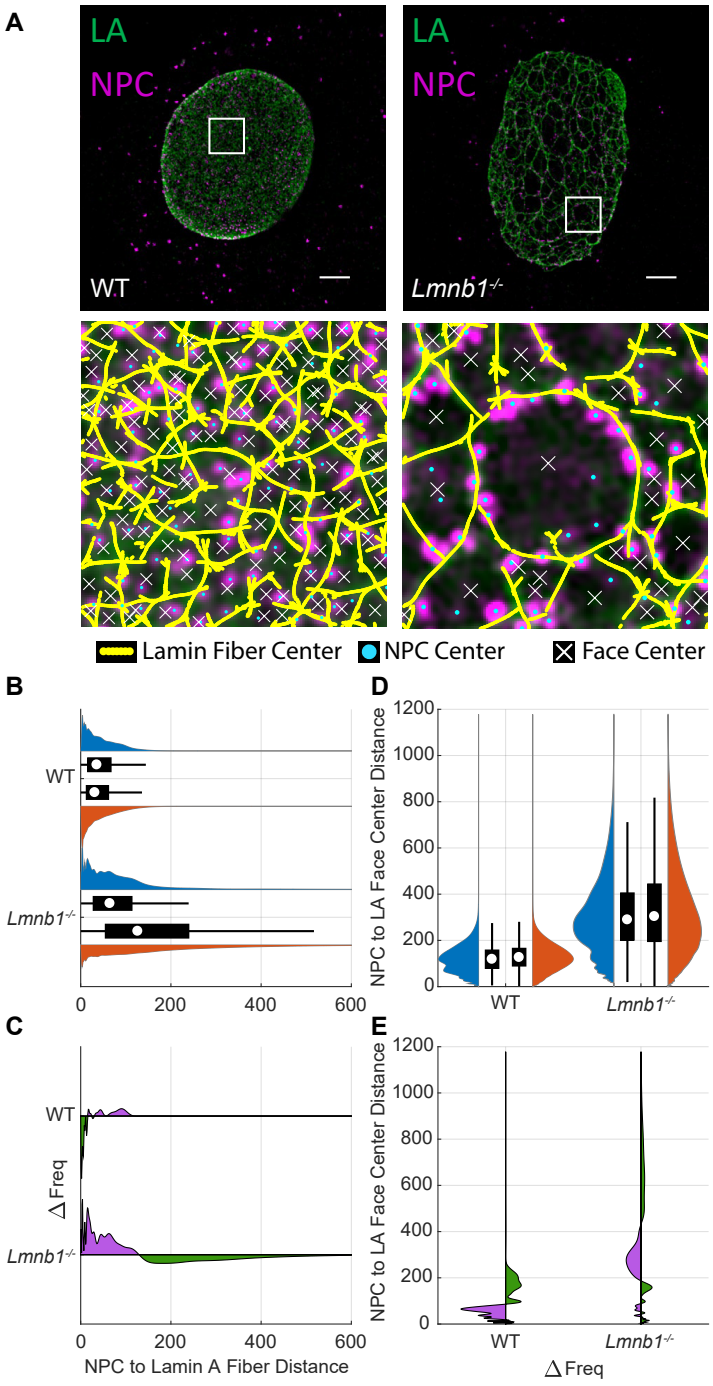

Figure 2. Computational Image Analysis of Lamin A and NPCs in Individual Nuclei A) Immunofluoresence images labeling LA (green) and NPCs (magenta) of wt and Lmnb1-/- MEF nuclei as in Figure 1 were subjected to computational image analysis. White boxes in the top row are magnified 8 times along each edge. The centers of LA fibers (yellow dots), NPCs (cyan dots), and faces (white Xs) were segmented to subpixel precision. Scale bar is 5 μm. B) Paired violin and box plots of NPC to LA fiber distances for the nuclei in (A). The violin (blue) and box plots on top represent the observed distance distributions. The violin (red) and box plots on bottom represent the expected distance distributions under the null hypothesis. The white circle indicates the median. The thick black bar indicates the interquartile range (IQR). The black whiskers indicate 1.5 times the IQR. C) Frequency difference plot of observed minus expected LA fiber to NPC distances. The green portion below the line indicates where the observed frequency is less than expected. The purple portion above the line indicates where the observed frequency is greater than expected. D) NPC to LA face center distances displayed as in (B), rotated 90 degrees counterclockwise. E) Frequency difference plot of NPC to LA face center distances, displayed as in (C), rotated 90 degrees counterclockwise.

Figure 2–Figure supplement 1. Bivariate histograms of LA Fiber-NPC and Face Center-NPC Distances in Single Nuclei. Illustration of Distances.

between the centers of LB2 fibers and NPCs (27.6 nm observed; -0.6 nm vs expected; $p < 0.001$; Table 1A, Figure 3A, Figure 3 - Figure Supplement 1D). However, the shift was an order of magnitude less and in the opposite direction than observed for LA and LB1 fibers. The median distance from NPCs to LB2 face centers (116.7 nm observed; -0.6 nm vs expected; Table 1A, Figure 3C) was not significantly different from expected. These findings suggest that there is no obvious relationship between the distribution of LB2 fibers and the distribution of NPCs, or if there is, it cannot be discerned in our analyses.

Knocking out *Lmna* affects the LB1-NPC relationship more than knocking out *Lmnb1* affects the LA-NPC relationship

The results presented in the previous section showed a clear spatial relationship between both LA and LB1 fibers and NPCs in the dense meshworks of WT MEF nuclei. The removal of either LA/C or LB1 by gene knockout in MEFs leads to dramatic changes in the remaining lamin meshwork characteristics, most notably an increase in the lamin mesh size (Figure 1B and Shimi et al 2015). Because the lamin fibers have close structural relationships with NPCs, we next wanted to determine if these relationships are altered when the lamin meshwork structure changes.

We analyzed the spatial relationships between LA fibers and NPCs in 10 *Lmnb1*$^{-/-}$ nuclei using the same quantitative methods applied to our studies of WT nuclei. In *Lmnb1*$^{-/-}$ nuclei, there was a greater median distance between LA fiber centers and NPC centers than expected (45.1 nm observed; +2.7 nm vs expected; Table 1A, Figure 3A, Figure 3 - Figure Supplement 2A), however, this shift in medians was not statistically significant ($p = 0.59$, Table 1A). Interestingly a statistical test comparing the standard deviations showed that the distributions are significantly different (48.6 nm observed; -168.2 nm vs expected; $p < 0.001$; Table 1A, Figure 3A, B). This reflects the long tail of the expected distributions, since under the null hypothesis some NPCs may appear in the middle of the faces of the enlarged LA meshworks, that is, farther away from the lamin fibers. The median distance of NPCs from the LA face centers was less than expected by a large magnitude (124.0 nm; -22.0 nm vs expected; $p < 0.001$; Table 1B; Figure 3C, D). This difference is due to the distribution of the offsets of the NPCs from the lamin fibers, which is larger than the expected offset distributions where more NPCs were closer to the lamin fibers. The observed distance distributions of WT and *Lmnb1*$^{-/-}$ MEFs (Figure 3A) both differ from the expected distributions under the null hypothesis in a similar manner (Figure 3B). This indicates that in *Lmnb1*$^{-/-}$ nuclei the proximal lateral relationship between LA fibers and NPCs remains although the median distance between LA fibers and NPCs increased by 5 nm. Overall, this suggests that the distance between the centers of LA fibers and NPCs does not depend strongly on the presence of LB1 fibers.

The results showed a relationship similar to LA fibers in WT MEFs for distances less than 30 nm where NPCs occurred less frequently than expected (green area; Figure 3B) and more frequently than expected around 50-100 nm (purple area; Figure 3B). This differed from the analysis of the single nucleus which consisted mostly of enlarged faces (Figure 2A), whereas most nuclei typically had a mix of small and large faces (Figure 1B).

Interestingly, the median distances between the centers of LB1 fibers and NPCs in *Lmna*$^{-/-}$ MEFs matched the expected distribution (34.9 nm observed; -0.8 vs expected; $p < 0.001$; Table 1A, Figure 3 A,B, Figure 3 – Figure Supplement 2B). Recall that in contrast, the LB1 fiber to NPC median distances in WT MEFs were slight larger and differed from the expected (38.1 nm; $p < 0.001$; Table 1A, Figure 3A). Additionally, the difference between the frequencies of the observed and expected distributions were smaller in magnitude in *Lmna*$^{-/-}$ MEFs compared to WT MEFs along with a small positive peak suggesting some colocalization (Figure 3B). The standard deviation of LB1 fiber to NPC medians in *Lmna*$^{-/-}$ MEFs did differ significantly from expected (34.9 nm observed; -263.1 nm vs expected; $p < 0.01$; Table 1A, Figure 3A, B) reflecting the enlarged faces in *Lmna*$^{-/-}$ MEFs. LB1 face center to NPC center distances were significantly different from expected with a large change in magnitude (122.1 nm observed; -11.1 nm vs expected; $p < 0.001$; Table 1B, Figure 3C, D). As in WT MEFs, this reflects a lateral proximal relationship between LB1 fibers and NPCs in *Lmna*$^{-/-}$ MEFs.

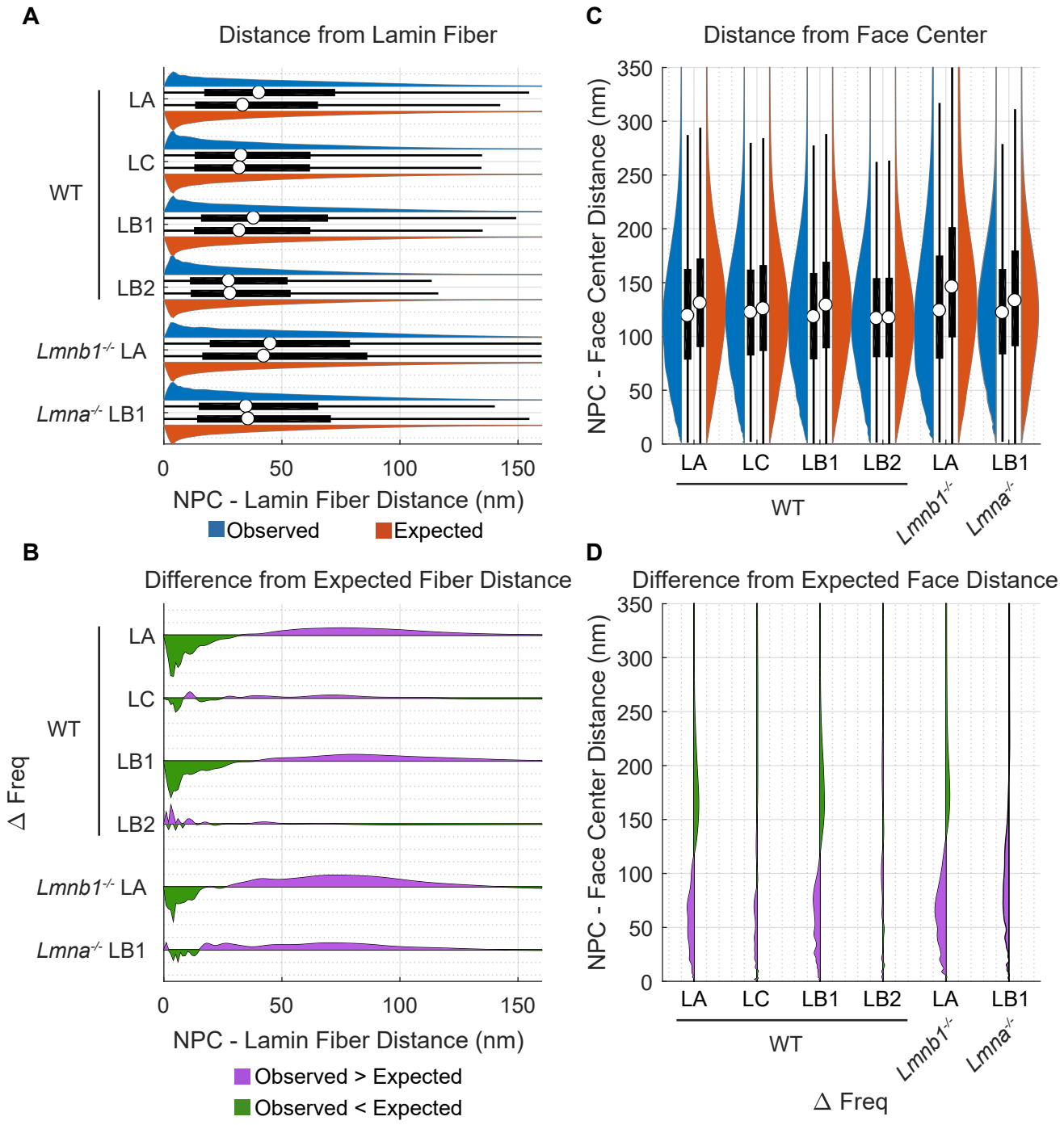

Figure 3. Quantitative Analysis of Lamin-NPC Distances A) Paired violin and box plots of NPC to lamin fiber distances. The violin (blue) and box plots on top represent the observed distance distributions. The violin (red) and box plots on bottom represent the expected distance distributions under the null hypothesis. The white circles indicate the medians. The thick black bar indicates the interquartile range (IQR). The black whiskers indicate 1.5 times the IQR. B) Frequency difference plots of observed minus expected lamin fiber to NPC distances. The green portion below the line indicates where the observed frequency is less than expected. The purple portion above the line indicates where the observed frequency is greater than expected. C) NPC to lamin face center distances displayed as in (A), rotated 90 degrees counterclockwise. D) Frequency difference plot of NPC to lamin face center distances, displayed as in (C), rotated 90 degrees counterclockwise.

Figure 3–Figure supplement 1. Bivariate histograms of WT MEFs

Figure 3–Figure supplement 2. Bivariate histograms of *Lmnb1*$^{-/-}$ and *Lmna*$^{-/-}$ MEFs

Figure 3–Figure supplement 3. Violin plots comparing the number of NPCs detected in WT *Lmna*$^{-/-}$ and *Lmnb1*$^{-/-}$ MEFs

The average number of NPCs per nucleus in a single focal plane was reduced to 1000 NPCs in *Lmna*$^{-/-}$ MEFs compared to 1200 in *Lmnb1*$^{-/-}$ MEFs and 1500 in WT MEFs (Table 1, Figure 3 - Figure Supplement 3).

Cryo-electron tomography (Cryo-ET) and immunogold labeling reveals lamin filaments contacting the nucleoplasmic ring of NPCs

In order to further investigate the relationship between lamin filaments and NPCs, we carried out cryo-ET of WT MEFs coupled with immunogold labeling of both LA and LB1. We hypothesized that this may shed additional insights on the lamin-NPC interaction and could reflect the relative abundance of LA and LB1 filaments contacting the NPC. We extracted 340 nm x 340 nm x 20 nm subtomograms around the nucleoplasmic ring of NPCs (Figure 4A; ***Turgay et al.*** (***2017***)) and counted the number of LA/C or LB1 filaments (Figure 4B). We observed more LA/C filaments than LB1 filaments in these regions (Figure 4C). These results also demonstrate that both LA and LB1 fibers are closely associated with the nucleoplasmic ring.

Depletion of the nucleoporins ELYS or TPR modifies the spatial relationship of LA fibers and NPCs in WT MEFs

The cryo-ET observations, taken together with the demonstration that there was a proximal lateral association between NPCs and both LA and LB1 fibers suggested that there are attachments of lamin filaments to nucleoplasmic components of NPCs. We next explored the potential roles of individual nucleoporins in attaching lamin fibers to the NPCs. For these studies we focused on ELYS, NUP153 and TPR, all components of the nucleoplasmic NPC structures that are in close proximity to the lamina (***Roux et al., 2012***). The nucleoporin ELYS is a component of the nucleoplasmic ring of NPCs and is required for post-mitotic NPC assembly where it binds to the chromosomes and recruits the Nup107-160 complex of the nucleoplasmic ring (***Franz et al., 2007***). TPR and Nup153 are both components of the nuclear basket structure of the NPC tht associates with the nucleoplasmic ring (***Duheron et al., 2014***; ***Krull et al., 2004***). We employed siRNA knockdown of each nucleoporin to determine their potential roles in linking the NPC to lamin fibers (Figure 5- Figure Supplement 1). We evaluated the efficacy of the knockdown by Western blot of whole cell lysates resulting in reductions of amount of each protein by 75%, 50%, or 40% for NUP153, ELYS, or TPR, respectively (Figure 5- Figure Supplement 2). Knockdown of either ELYS or TPR led to significant changes in NPC distribution and structural relationship to the LA fibers. The most dramatic effect was the reorganization of NPCs into clusters after ELYS knockdown (Figure 5A). Individual fluorescent puncta could still be resolved within each cluster indicating that some NPC structure was likely retained. In contrast, siRNA knockdown of NUP153 or TPR did not cause NPC clustering in WT MEFs (Figure 5A). The median distance between the centers of NPCs and LA fibers in ELYS depleted cells (70.8 nm; +20 nm vs scrambled; $p < 0.001$; Table 2A, Figure 5A, B, Figure 5- Figure Supplement 1) increased compared to scrambled siRNA controls (50.9 nm; $p < 0.001$; Table 2A, Figure 5A, B, Figure 5- Figure Supplement 1). Additionally, the median distance between face centers of the LA fiber meshwork and the NPCs was reduced (89.7 nm; Table 2B; Figure 5C) compared to scrambled siRNA (106.2 nm; $p < 0.001$; Table 2B, Figure 5C, Figure 5- Figure Supplement 1). These data suggested that LA fibers were being excluded from the ELYS depleted NPC clusters such that these clusters became located in large faces within the LA meshwork. Interestingly, the size of faces contained within the LA meshwork also appeared to increase upon ELYS knockdown (Figure 5A). As a measure of lamin face size, we summed the NPC to fiber distances and the NPC to face center distances, since, for a perfectly circular face in the meshwork, this quantity would be the radius of the circle with respect to each NPC. The face radius of the LA fiber meshwork (169.7 nm; Table 2C) significantly increased versus the scrambled siRNA control (163.3 nm; $p < 0.001$; Table 2C) upon ELYS knockdown indicating that the LA meshwork expanded when ELYS was depleted.

While there did not appear to be NPC clustering upon TPR depletion, the NPCs appeared to be less associated with the LA fibers and more centered within the faces of a dense LA meshwork

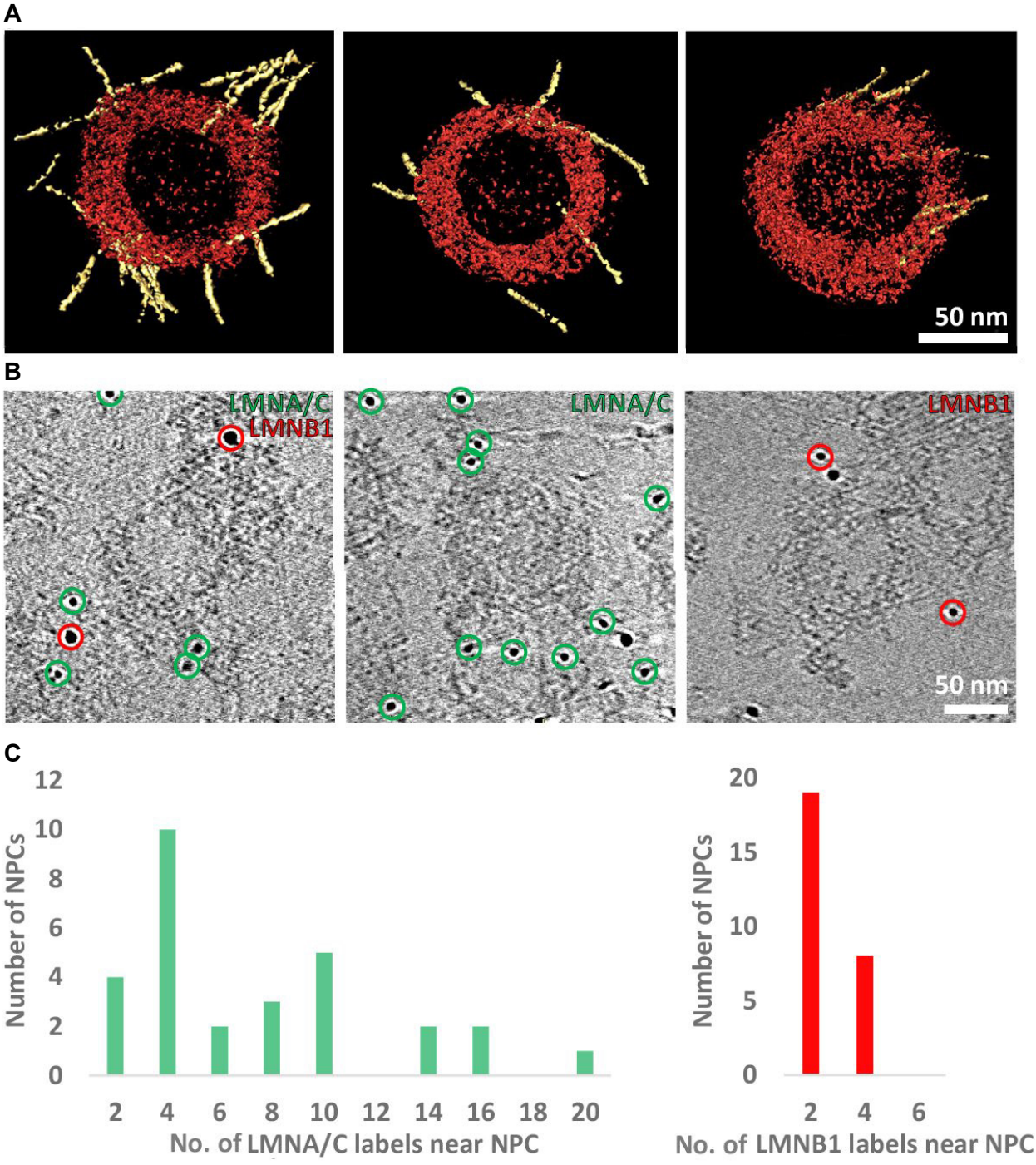

Figure 4. Cryo-Electron Tomography Showing LA/C and LB1 Filament Contacts with the Nucleoplasmic Ring Enrichment of LA/C over LB1 around the nucleoplasmic ring of NPCs. A) Lamin filaments (yellow) interact with NPCs (red) as seen by surface rendering representations of cryo-sub-tomograms. B) Gold labelling of lamin filaments observed by cryo-ET. The position of Lamin A/C labels (green) and Lamin B1 labels (red) are indicated. Double labeling (left) or labeling of individual lamin isoform were analyzed and presented as histograms. The unmarked gold particles (B-middle, right) are fiducial markers. C) A total number of 214 Lamin A/C labels and 70 Lamin B1 labels were detected around 47 nucleoplasmic rings.

(Figure 5A). The median distance between the centers of NPCs and LA fibers with TPR silencing (59.0 nm; Table 2A, Figure 5 B,C, Figure 5- Figure Supplement 1) increased versus a scrambled siRNA control, though to a lesser magnitude than for ELYS knockdown (+8.2 nm TPR KD vs +20.0 nm ELYS KD; $p < 0.001$; Table 2A, Figure 5 B,C). The median distance between NPCs and LA face centers (90.0 nm; Table 2B, Figure 5D) was reduced with TPR silencing (-16.2 nm; $p < 0.001$; Table 2B, Figure 5 D, E). The face radius of the LA fiber meshwork (154.3 nm; $p < 0.001$; Table 2C) was decreased upon TPR depletion (-9.1 nm; $p < 0.001$; Table 2C). These data suggested that the NPCs were less closely associated with LA fibers following TPR knockdown. Additionally, the reduced face size suggested that the LA meshwork faces were reduced in size (e.g., compacted) upon TPR knockdown forcing NPCs into more confined spaces than in WT LA meshworks.

In contrast to ELYS and TPR knockdowns, NUP153 knockdown only slightly reduced the median distance between NPCs and LA fibers (-0.8 nm; $p < 0.001$; Table 2A, Figure 5B, C). This reduction was an order of magnitude smaller than observed for the knockdown of either ELYS or TPR. The distance between LA face centers and NPCs was reduced (-6.5 nm; $p < 0.001$; Table 2B, Figure 5 D, E, Figure 5- Figure Supplement 1) and the face radius for the LA meshwork was reduced (-7.5 nm; $p < 0.001$; Table 2C). The faces in the LA meshwork also appeared smaller and more compact compared to controls which was similar to the effect seen with TPR knockdown.

Depletion of ELYS or TPR modifies the spatial relationship of LC fibers and NPCs

Our analysis of LC fibers and NPCs suggested that LC fibers do not have a definable relationship with NPCs in WT MEFs (see Figure 3). However, the co-distribution of LC fibers and NPCs was significantly modified by knockdown of either ELYS or TPR. ELYS knockdown resulted in an increase in the median distance between NPCs and LC fibers (63.1 nm; +20.2 nm vs scrambled; $p < 0.001$; Table 2A, Figure 6 A,B,C, Figure 6- Figure Supplement 1) and the LC face center to NPC center distances decreased (96.1 nm; -13.0 nm vs scrambled; $p < 0.001$; Table 2B, Figure 6 D,E). The knockdown of ELYS also increased the effective face radius (167.5 nm; +10.5 nm vs scrambled; $p < 0.001$; Table 2C) indicating that ELYS silencing results in expanded LC meshworks as it did for LA meshworks. These results suggest that the NPC clusters induced by ELYS depletion exclude LC fibers as well as LA fibers.

siRNA knockdown of TPR resulted in an increase in the median distance between NPCs and LC fibers (+13.7 nm vs scramble; $p < 0.001$; Table 2A, Figure 6B, C, Figure 6- Figure Supplement 1), a decrease in median distances between NPCs and LC face centers (-19.2 nm; $p < 0.001$; Table 2B, Figure 6 D,E) and a decrease in the effective face radius (-6.2 nm; Table 2C; $p < 0.001$). These results indicate that the LC meshwork face size decreased after TPR knockdown, similar to LA.

NUP153 knockdown resulted in a decrease (-3.0 nm; $p < 0.001$; Table 2A, Figure 6 B, C, Figure 6- Figure Supplement 1) in the median distance between NPCs and LC fibers. Decreases in LC face to NPC center distances (-2.2 nm; $p < 0.0.01$; Table 2B, Figure 6 D,E) and face radius were also detected (-4.1 nm; $p < 0.001$; Table 2C). While these decreases are consistent with the change seen in the distances between NPCs and LA fibers, the magnitude of the change is much less than for depletion of ELYS or TPR. Overall, the observed changes in the NPC distribution relative to LC fibers upon ELYS, TPR, and NUP153 knockdown were similar to those observed for LA fibers.

Depletion of TPR, NUP153, or ELYS changes the spatial relationship of LB1 fibers and NPCs

Depletion of TPR, NUP153, or ELYS altered the median center-to-center distance between LB1 fibers and NPCs (+0.5 nm, -4.7 nm, and -3.1 nm, respectively, Obs. – Scram; $p < 0.001$; Table 2A, Figure 7A, B, Figure 7- Figure Supplement 1) relative to scrambled siRNA controls. The small magnitude of these changes suggests that depletion of these nucleoporins had a minimal impact on the relationship between LB1 and NPCs compared to the changes seen in the distances between NPCs and LA/C fibers (Figure 7C). In contrast, the changes in median distance between LB1 face centers and NPCs were larger in magnitude upon knockdown of TPR, NUP153, or ELYS (-19.2 nm,

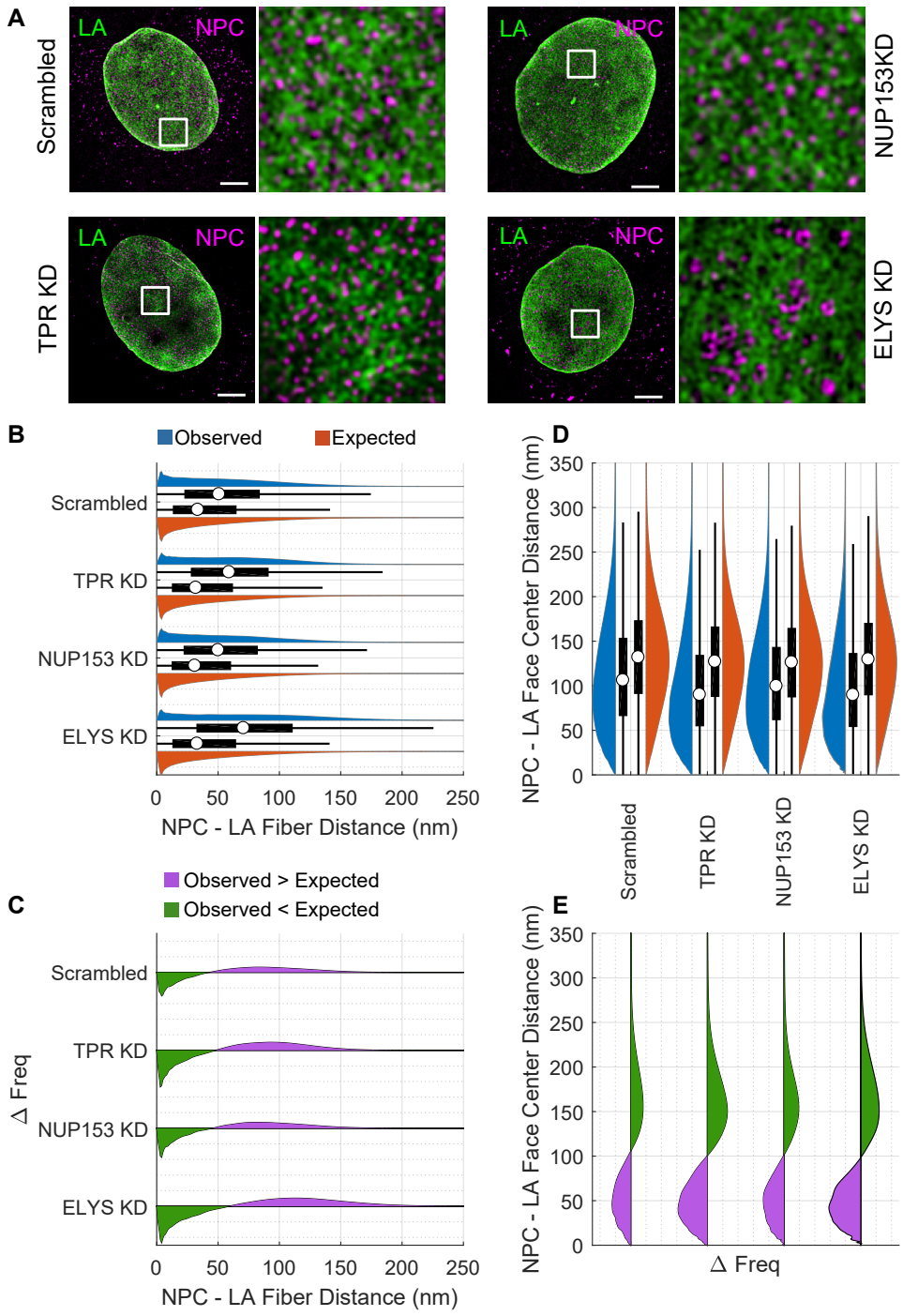

Figure 5. Co-distribution of LA and NPC components after siRNA Transfection. A) Immunofluorescence images of LA (green) and NPCs (magenta) following knockdowns (KD) of TPR , NUP153, ELYS and scramble control. Note the clustering of NPCs in the ELYS KD. Scale bar = 5 μm. B) Paired violin and box plots of NPC center to LA fiber center distances. The violin (blue) and box plots represent the observed distance distributions. The violin (red) and box plots on bottom represent the expected distance distributions under the null hypothesis. The white circle indicates the median. The thick black bar indicates the interquartile range (IQR). The black whiskers indicate 1.5 times the IQR. C) Frequency difference plots of observed minus expected LA fiber to NPC distances for the silencing series. The green portion below the line indicates where the observed frequency is less than expected. The purple portion above the line indicates where the observed frequency is greater than expected. D) NPC center to LA face center distances displayed as in (B), rotated 90 degrees counterclockwise. E) Frequency difference plot of NPC to LA face center distances, displayed as in (C), rotated 90 degrees counterclockwise.

Figure 5–Figure supplement 1. Bivariate histograms of LA Fiber-NPC and Face Center-NPC Distances

Figure 5–Figure supplement 2. Western Blots of ELYS, NUP153, AND TPR siRNA Knockdown Experiments

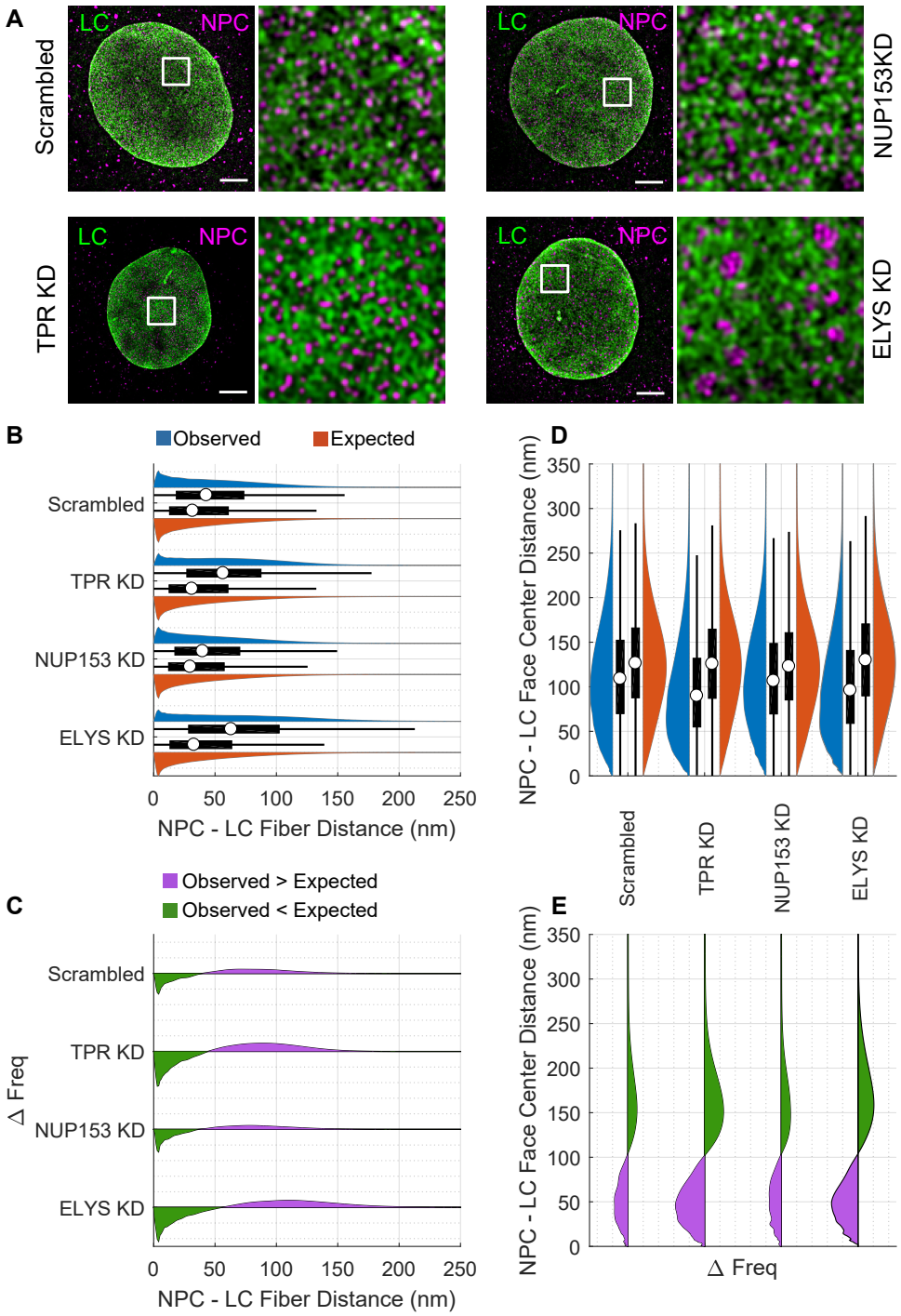

Figure 6. Co-distribution of LC and NPCs after siRNA Transfection. A) Double label immunofluoresence images of LC (green) and NPCs (magenta) following KDs of TPR, NUP153, ELYS and scramble control. Scale bar = 5 μm. B. Paired violin and box plots of NPC center to LC fiber center distances. The violin (blue) and box plots on top represent the observed distance distributions. The violin (red) and box plots on bottom represent the expected distance distributions under the null hypothesis. The white circle indicates the median. The thick black bar indicates the interquartile range (IQR). The black whiskers indicate 1.5 times the IQR. C) Frequency difference plots of observed minus expected LC fiber to NPC distances for the silencing series. The green portion below the line indicates where the observed frequency is less than expected. The purple portion above the line indicates where the observed frequency is greater than expected. D) NPC center to LC face center distances displayed as in (B), rotated 90 degrees counterclockwise. E) Frequency difference plot of NPC center to LC face center distances, displayed as in (C), rotated 90 degrees counterclockwise.

Figure 6–Figure supplement 1. Bivariate histograms of LC Fiber-NPC and Face Center-NPC Distances

-2.5 nm, and -13.0 nm, respectively; Obs. – Scram.; $p < 0.001$; Table 2B, Figure 7 D, E, Figure 7-Figure Supplement 1) ; and face radii decreased (-20.3 nm, -1.1 nm, -17.6 nm; Obs. – Scram.; $p < 0.001$; Table 2C). Knocking down TPR or ELYS decreased the distances between NPCs and LB1 face centers as well as the LB1 face radii, while knocking down NUP153 had less impact.

Depletion of ELYS, TPR, or Nup153 has a minor impact on the independence between LB2 fibers and NPCs

As described in previous sections, we could not detect a relationship between LB2 fibers and NPCs in WT MEFs (see Figure 3). Upon knockdown of TPR, NUP153, or ELYS, the observed distances between LB2 fibers and NPCs differed by a few nanometers from expected (-1.7 nm, -6.6 nm, and +3.0 nm, respectively; Obs.- Exp., $p < 0.01$; Table 2A, Figure 8A,B, Figure 8- Figure Supplement 1) and from the scramble control (-1.5 nm, -4.4 nm, and +4.1 nm, respectively; Obs. - Scram; $p < 0.01$; Table 2A, Figure 8A,B,C). Although the changes in association between the NPCs and LB2 fibers were minimal, the differences were statistically significant with NUP153 knockdown having the greatest effect. In contrast, LB2 face center to NPC center distances (-13.6 nm, +0.9 nm, and -18.2 nm vs scrambled; Obs. – Scram.; $p < 0.01$; Table 2B; Figure 8D,E) and the face radii decreased significantly (-16.4 nm, -4.9 nm, -14.8 nm vs scrambled; Obs. – Scram; $p < 0.01$; Table 2C, , Figure 8-Figure Supplement 1), following knockdown of TPR, NUP153, or ELYS, respectively. Thus, the main effect of the TPR and ELYS knockdown was to decrease the LB2 face radii and the distance to the LB2 face centers relative to the NPC distribution. In contrast, the LB2 fiber to NPC center distances were not perturbed to the same extent when compared to the other lamin fibers.

NPC changes in *Lmna*$^{-/-}$ and *Lmnb1*$^{-/-}$ MEFs after nucleoporin knockdown

In addition to the NPC clustering following ELYS knockdown in WT MEFs (Figure 5A), we observed similar NPC clustering following ELYS knockdown in *Lmna*$^{-/-}$ and *Lmnb1*$^{-/-}$ MEFs (Figure 8 - Figure Supplement 2A). This suggest the clustering effect induced by ELYS depletion is not strongly dependent on the presence of LA/C or LB1.

NUP153 knockdown had modest effects on the relationship of NPC to lamin fiber distances and lamin meshwork sizes in WT cells. However, we did observe clustering of NPCs in *Lmna*$^{-/-}$ and *Lmnb1*$^{-/-}$ upon silencing of NUP153 (Figure 8 - Figure Supplement 2B).

With TPR knockdown we did not see an increase in the number of NPCs or clustering compared to scrambled siRNA in WT MEFs (Figure 8 - Figure Supplement 2C,D). The only change in the number of NPCs in WT MEFs was upon ELYS KD, but this may be due to our inability to resolve individual NPCs in the the clusters that formed ($p < 0.01$). However, the shape of the distribution of the number of NPCs following TPR knockdown was altered in *Lmnb1*$^{-/-}$ MEFs due to an increased proportion of cells showing a similar number of NPCs as WT MEFs, suggesting that effects on the number of pores following TPR KD may be dependent on the amount of LB1 present in the cell (Figure 8 - Figure Supplement 2D). However, across the ten cells analyzed, the change in the median number of NPCs observed in *Lmnb1*$^{-/-}$ MEFs was not significant changed upon TPR KD versus scramble control (Figure 8 - Figure Supplement 2D).

Discussion

Lamins and nucleoporins assemble into the nuclear lamina and NPCs within the nuclear envelope and have unique functions critical for cellular function including gene expression and genome maintenance, mechanotransduction, mitosis and a host of other activities. However, the structural and functional interactions between the NL and NPCs are relatively understudied and the potential cooperativity between these structures is largely unknown. In this study, we have focused on the structural association between the NL and NPCs.

Our 3D-SIM imaging and image analysis of MEFs has revealed important insights into the structural relationship between the lamin fibers and NPCs. Removing either LA/C or LB1 from the NL

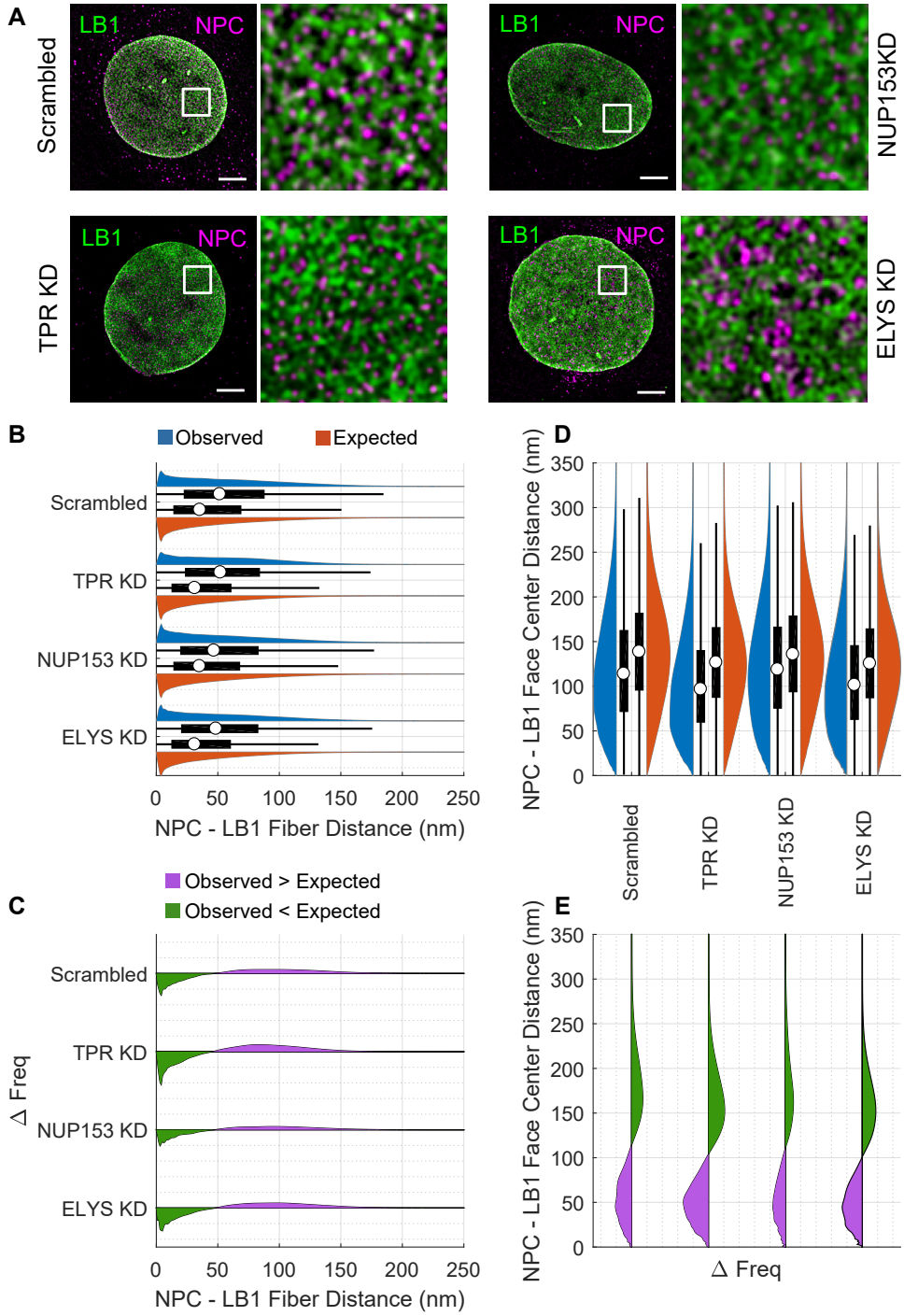

Figure 7. Co-distribution of LB1 and NPCs after siRNA Transfection. A) Double label immunofluoresence images of LB1 (green) and NPCs (magenta) following KDs of TPR, NUP153, ELYS and scramble control. Scale bar = 5 μm. B) Paired violin and box plots of NPC center to LB1 fiber center distances. The violin (blue) and box plots on top represent the observed distance distributions. The violin (red) and box plots on bottom represent the expected distance distributions under the null hypothesis. The white circle indicates the median. The thick black bar indicates the interquartile range (IQR). The black whiskers indicate 1.5 times the IQR. C) Frequency difference plot of observed minus expected LB1 fiber to NPC center distances for the silencing series. The green portion below the line indicates where the observed frequency is less than expected. The purple portion above the line indicates where the observed frequency is greater than expected. D) NPC center to LB1 face center distances displayed as in (B), rotated 90 degrees counterclockwise. E) Frequency difference plot of NPC to LB1 face center distances, displayed as in (C), rotated 90 degrees counterclockwise.

Figure 7–Figure supplement 1. Bivariate histograms of LB1 Fiber-NPC and Face Center-NPC Distances

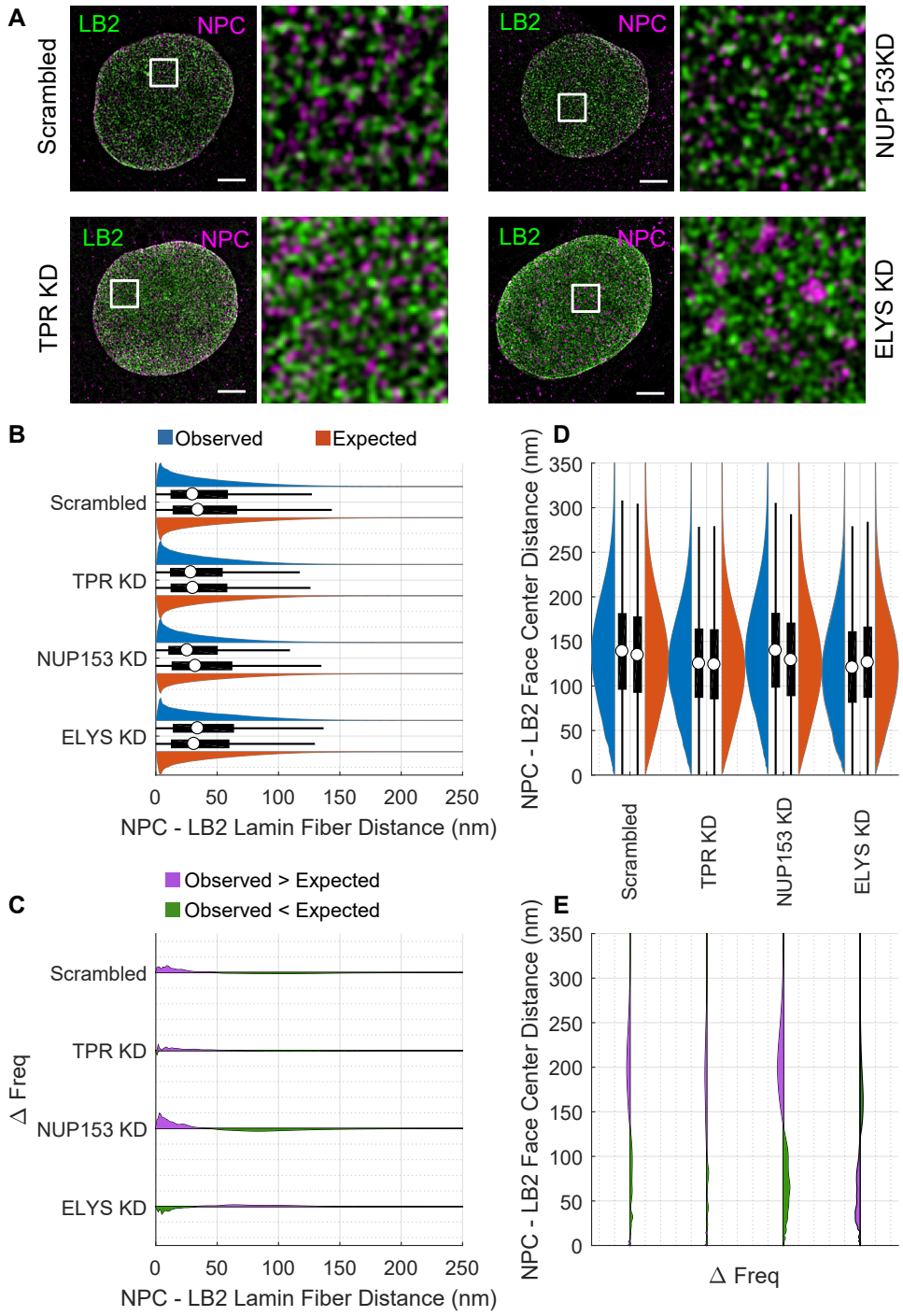

Figure 8. Co-distribution of LB2 and NPCs after Silencing Nucleoporins A) Immunofluorescence images of LB2 (green) and NPCs (magenta) following KDs of. TPR, NUP153, ELYS and scramble control. Scale bar = 5 μm. B) Paired violin and box plots of NPC center to LB2 fiber center distances. The violin (blue) and box plots on top represent the observed distance distributions. The violin (red) and box plots on bottom represent the expected distance distributions under the null hypothesis. The white circle indicates the median. The thick black bar indicates the interquartile range (IQR). The black whiskers indicate 1.5 times the IQR. C) Frequency difference plot of observed minus expected LB2 fiber center to NPC center distances. The green portion below the line indicates where the observed frequency is less than expected. The purple portion above the line indicates where the observed frequency is greater than expected. D) NPC center to LB2 face center distances displayed as in (B), rotated 90 degrees counterclockwise. E) Frequency difference plot of NPC to LB2 face center distances, displayed as in (C), rotated 90 degrees counterclockwise.

Figure 8–Figure supplement 1. Bivariate histograms of LB2 Fiber-NPC and Face Center-NPC Distances

Figure 8–Figure supplement 2. Effect of ELYS, NUP153, and TPR KD in *Lmnb1*$^{-/-}$ and *Lmna*$^{-/-}$ MEFs

by gene knockout causes the enlargement of meshwork faces (***Shimi et al., 2015***) accompanied by the NPC localization to the perimeter of lamin meshwork faces and the decrease in NPC density (Figure 1B and 1C), indicating that LA/C and LB1 are required for maintaining the normal NPC distribution/density. These results have led to the idea that nascent NPCs are formed in close proximity to lamin fibers and/or existing NPCs are stably anchored to lamin fibers. To support this idea, we have observed by cryo-ET that lamin filaments appear to have a direct contact with the outer ring or basket of NPCs (Figure 4) as supported by biochemical evidence suggesting that the lamin filament-NPC association is relatively strong (***Kay et al., 1972***; ***Dwyer and Blobel, 1976***; ***Scheer et al., 1976***). It is possible that LA/C or LB1 KO reduces the mass of lamin filaments/fibers to provide less anchorage sites for NPCs.

Based on our results, specific nucleoporins are involved in maintaining the normal lamin mesh hole size and NPC distribution/density. ELYS is a component of the Nup107-160 complex located at the outer ring of the NPC (***Rasala et al., 2006***) and is in close proximity to LA in the NL (***Roux et al., 2012***). ELYS KD induces the formation of NPC clusters within enlarged LA/C meshwork faces, leading to the disruption of the normal lamin fiber-NPC association (Figure 5-8). It is too difficult to check the ELYS KD effect on NPC density because single NPCs within each cluster cannot be resolved by 3D-SIM (Figure 5-8). These results strongly suggest the lamin association with ELYS mediates the structural relationship between the lamin filaments/fibers and NPCs. In mammalian cells, the NL and NPCs disassemble at the nuclear envelope break down (NEBD) and reassemble during cell division. The disassembly and reassembly of the NL and NPCs are considered to be coupled to the phosphorylation and dephosphorylation of lamins, nuclear membrane proteins and nucleoporins (***Gerace and Blobel, 1980***; ***Peter et al., 1990***; ***Dessev et al., 1991***; ***Foisner and Gerace, 1993***; ***Macaulay et al., 1995***; ***Favreau et al., 1996***). ELYS is accumulated on the surface of the chromosome mass at the early stage of the NE reassembly to recruit other nucleoporins, nuclear membrane proteins and lamins to the NE (***Rasala et al., 2006***). Because ELYS KD causes defects in reassembling nucleoporins and nuclear membrane proteins to the NE (***Rasala et al., 2006***; ***Doucet et al., 2010***), NPC clusters and enlarged meshwork faces might be formed during the NE reassembly. In its absence other molecules such as the other lamin isoforms may be separating NPCs from LA fibers.

We show that the effects of TPR KD are almost opposite from those of ELYS KD, decreasing lamin mesh hole size (Figure 5-8). It has been reported that NPC density is increased by TPR KD because TPR provides a scaffold for ERK1/2 to phosphorylate Nup153 in the nuclear basket of NPCs, which is critical for early stages of NPC biogenesis (***McCloskey et al., 2018***). TPR KD reduces the phosphorylation of Nup153 to slow NPC biogenesis down, causing the accumulation of NPCs. On the other hand, a mechanism for tightening lamin meshworks by TPR KD is totally unknown. Though we do not detect an increase in lamin expression by western blotting, the mass of lamin filaments/fibers might be locally changed by the unknown mechanism (data not shown). Mitotic phosphorylation sites of lamins are phosphorylated during interphase and involved in regulating the exchange of lamins between the NL and nucleoplasm (***Kochin et al., 2014***). It is possible that TPR contributes to phosphorylate adjacent lamins through the ERK-MAPK pathway to control lamin exchange proximal to NPCs. TPR KD might cause the accumulation of lamin filaments/fibers, consequently providing more anchorage sites for NPCs.

The functional aspect of the structural association between the NL and NPCs that we describe in this study still remain unclear. Electron microscopic studies have revealed that the NL associates with heterochromatin while NPCs associate with euchromatin (***Fawcett, 1966***; ***Ou et al., 2017***). Moreover, genomic studies indicate that lamina-associated domains (LADs) are silenced for transcription while nucleoporin-associated regions (NARs) are transcriptionally permissive (***Guelen et al., 2008***; ***Toda et al., 2017***). The contacting surfaces of the lamin filaments/fibers with NPCs should correspond to the boundaries between these different chromatin structures, which implies that the boundaries facilitate distinct functions of these chromatin structures.

Over 500 mutations in the LMNA gene cause human diseases, collectively termed laminopathies.

LA/C KO mice exhibit disease phenotypes including muscular dystrophy, cardiomyopathy and peripheral neuropathy before death at 6-8 weeks, partially mimicking a subpopulation of human laminopathies (***Sullivan et al., 1999***; ***Kim and Zheng, 2013***). As fibroblasts from patients carrying a LMNA mutation (G608G) causing Hutchinson-Gilford progeria syndrome (HGPS) exhibit distortion of the NL structure, misshaping of their nuclei and redistribution of NPCs (***Goldman et al., 2004***). LB1 KO causes perinatal lethality in mice attributable to developmental defects in the forebrain, bone and lung (***Vergnes et al., 2004***; ***Kim et al., 2011***); whereas the LB2 KO involves less severe defects in forebrain development compared to the LB1 KO mice (***Kim et al., 2011***). The majority of the underlining mechanisms in which these lamin-deficiencies cause laminopathies and other defects has yet to be determined. Our findings may shed new light on physiological and pathological significance of the reciprocal relationship between the lamin filaments/fibers and NPCs

Materials and Methods

Cell culture

Immortalized WT, *Lmna*$^{-/-}$, *Lmnb1*$^{-/-}$, and *Lmnb2*$^{-/-}$ MEFs were cultured as previously described (***Shimi et al., 2015***). Briefly, cells were cultured in modified DMEM (Thermo Fisher Scientific, Waltham, MA, USA) supplemented with 10% fetal calf serum, 50 U/ml penicillin G, 50 μg/ml streptomycin sulfate (Thermo Fisher Scientific) at 37°C in a humidified CO2 incubator.

Super resolution microscopy

3D-SIM was carried out as previously described (***Shimi et al., 2015***). Briefly, a Nikon Structured Illumination Super-resolution Microscope System (Nikon N-SIM; Nikon, Tokyo, Japan) was built on an ECLIPSE Ti-E (Nikon) equipped with sCMOS camera ORCA-Flash 4.0 (Hamamatsu Photonics Co., Hamamatsu, Japan) and an oil immersion objective lens CFI SR (Apochromat TIRF 100×, NA=1.49, Oil, WD=0.12; Nikon). N-SIM was operated with NIS-Elements AR (Nikon). For image acquisition, 21 optical sections including a region of the lamina were taken at 50-nm intervals. For image reconstruction from the raw data, illumination modulation contrast, high-resolution noise suppression, and out-of-focus blur suppression were set with fixed values of 1, 0.75, and 0.25, respectively. For presentation, images were adjusted for brightness and contrast. Statistical values were determined using Student's t test.

Indirect immunofluorescence

Samples for indirect immunofluorescence were processed as previously described (Shimi et al., 2015). Cells were seeded on Gold Seal coverglasses (22 × 22 mm2, no. 1.5; Thermo Fisher Scientific) and fixed with methanol for 10 min at -20°C. Lamins were stained with rabbit polyclonal anti-LA (1:500; 323; ***Dechat et al.*** (***2007***)), goat polyclonal anti-LB1 (1:500; SC-6217; Santa Cruz Biotechnology, Dallas, TX, USA), and rabbit monoclonal LB2 (1:100; EPR9701(B); Abcam, Cambridge, MA, USA), and rabbit polyclonal anti-LC (1:500; 321; ***Dechat et al.*** (***2007***)). Nucleoporins were stained with mouse monoclonal MAb414 (1:1000; BioLegend, San Diego, CA). The secondary antibodies used were donkey anti-mouse immunoglobulin G (IgG)–Alexa Fluor 488, donkey anti-mouse IgG–Alexa Fluor 568, donkey anti-rabbit IgG–Alexa Fluor 488, donkey anti-rabbit IgG–Alexa Fluor 568, donkey anti-goat IgG–Alexa Fluor 488, and donkey anti-goat IgG–Alexa Fluor 568 (all 1:500; Thermo Fisher Scientific). Processed coverslips were mounted with ProLong Diamond antifade reagent (Thermo Fisher Scientific).

RNA interference

ON-TARGETplus siRNA oligos (Dharmacon, Lafayette, CO, USA) were used for RNAi-mediated knockdown experiments.

Scrambled sequence for control siRNAs;

1. (D-001810-01) 5'-UGGUUUACAUGUCGACUAA-3'

Target	Antibody	Catalog #	Supplier	Host Species	Dilution
LA	323	***Dechat et al.* (*2007*)**	Goldman Lab	Rabbit	1/500
LC	321	***Dechat et al.* (*2007*)**	Goldman Lab	Rabbit	1/500
LB1	M20	sc-6217	Santa Cruz	Goat	1/500
LB2	EPR9701(B)	ab151735	Abcam	Rabbit	1/100
FXFG Rep. Nups	mAb414	902902	Biolegend	Mouse	1/1000

Primary Antibodies used for Immunofluorescence

2. (D-001810-02) 5′-UGGUUUACAUGUUGUGUGA-3′
3. (D-001810-03) 5′-UGGUUUACAUGUUUUCUGA-3′
4. (D-001810-04) 5′-UGGUUUACAUGUUUUCCUA-3′

Nup153 siRNAs;

1. (J-057025-11) 5′-CGCUAUGUGCAUUGAUAAA-3′
2. (J-057025-12) 5′-GGGACAGGCUUUGGAGAUA-3′

ELYS siRNA

1. (J-051465-09) 5′-CCACUGAACUAACUACUAA-3′
2. (J-051465-10) 5′-GGAAAGAAGAAGGACGUUA-3′

TPR siRNA;

1. (J-041152-09) 5′- CAACAAACAUUCAUCGGUA-3′
2. (J-041152-10) 5′- CGUGACAUGUACCGAAUUU-3′

5×10^4 MEFs were plated into each well of 6-well plates 24 h before transfection. 30 pmol of siRNA oligos was transfected onto the cells in each well with Lipofectamine RNAiMAX transfection reagents (Thermo Fisher Scientific), following the manufacturer's instructions. 48h after incubation at 37°C, the transfected cells were trypsinizedand replated at 5×10^4 cells/well into each well of 6-well plates and transfected with 30 pmol of the siRNA. 48h after incubated at 37°C, the transfected cells were trypsinized and replated on coverslips for indirect immunofluorescence or plated into a 60 mm dish for western blotting.

Quantitative blotting of anti-nucleoporin antibodies.

The linearity of antibodies to nucleoporins was determined by immunoblotting of whole cell lysates of WT MEFs. Five samples of MEF lysates containing between 7.5×10^3 to 9×10^3 cells were separated in duplicate lanes of a 7.5% SDS-polyacrylamide gel (SDS-PAGE) and transferred to nitrocellulose for immunoblotting. After transfer, the membrane was briefly rinsed in dH2O and stained with Revert Protein Stain (LI-COR) and imaged in an Odyssey Fc (LI-COR Biosciences, Lincoln NB) at 700nm. The membrane was then washed with TBS and blocked in 5% non-fat dry milk (NFM) in TBS for 1hr at room temperature and then in the same solution containing 0.1% Tween 20 for 30 minutes. For incubation with antibodies, the appropriate antibody was diluted in blocking solution with Tween at the indicated dilution (See Table Below) and incubated overnight at 4 °C with gentle agitation. The blots were washed 3X 5 mins each wash with TBS containing 0.1% Tween 20. For detection, the appropriate secondary antibodies (Licor IRDye 800CW) were diluted 1:15000 in 5% NFM containing 0.2% Tween 20 and incubated with the membrane for 1hr at room temperature with gentle agitation. The membranes were washed 3X 5 mins each with TBS containing 0.1% Tween 20 and allowed to dry. The dried membranes were imaged in an Odyssey Fc at 800nm.

Images of the total protein stain and specific antibody labeling were analyzed using Empiria Studio Software (LI-COR Biosciences, Lincoln NB). The intensity of the specific antibody labeling in each lane was corrected for protein load using the software and the linearity of the antibody response was determined by the software.

Target	Antibody	Catalog #	Supplier	Host Species	Concentration
Nup153	R3G1	sc-101544	Santa Cruz	Rat	200 $\mu g\,mL^{-1}$
Elys	bs-9880R	bs-9880R	Bioss	Rabbit	50 $\mu g\,mL^{-1}$
Tpr	ab84516	ab84516	Abcam	Rabbit	100 $\mu g\,mL^{-1}$

Antibodies used for Western blotting

The degree of knockdown for each nucleoporin was determined by SDS-PAGE by loading duplicate samples of each knockdown cell lysate such that the antibody response should be in a linear range, based on the analysis of wt lysates. For quantitation of knockdown, a dilution series of wt lysate was run on the same gel at concentrations that were expected to be in the linear range of the antibody response. After electrophoresis and transfer, the membranes were treated identically to the conditions for determining antibody linearity, imaged in the Odyssey Fc and the images analyzed using Empiria software.

NPC-lamin rendered view

Cryo-electron tomograms that were acquired previously (***Turgay et al., 2017***) were further analyzed. The central coordinates of NPCs within cryo-tomograms of NE were determined manually and sub-tomograms (340 nm x 340 nm x 20 nm) were reconstructed in MATLAB, using the TOM toolbox (***Nickell et al., 2005***). The lamin filaments and NPCs in 4 selected sub-volumes were segmented manually and rendered, using the Amira software package (Thermo Fisher Scientific).

Immunogold labelling image processing

Sub-tomograms of gold labeled lamins (***Turgay et al., 2017***) were reconstructed as described above (47 sub-tomograms). The subvolumes containing NPCs (in top-view orientation), were projected along the Z axis, to produce a 2D image. The coordinates of the gold clusters (6 nm and 10 nm) were identified manually and counted. The respective histograms were drawn in Excel (Microsoft).

Computational Image Analysis

Computational image analysis was done using MATLAB (Mathworks, Natick, MA) using custom software developed in the Jaqaman Lab. Nikon ND2 files containing image and meta data were loaded into MATLAB using Bioformats (Open Microscopy Environment, ***Linkert et al.*** (***2010***)). Nuclear pore complexes were detected and localized using an adapted pointSourceDetector routine from the lab of Gaudenz Danuser which involved two-dimensional local maxima deteciton, Gaussian fitting, and Gaussian mixture modeling. Lamin fibers were segmented using multi-orientation analysis as described in ***Kittisopikul et al.*** (***2019***) to accurately segment a meshwork structure with many junctions. Lamin fibers were further localized as in Appendix 1. The source is available on Github at https://github.com/mkitti/LaminNpcAnalysis

Computation was conducted on Northwestern University's high performance computing environment, Quest. Files were stored on Northwestern University Research Data Storage Service FSMRESFILES. Globus.org and Box.com were used to transfer files between storage and computational environments.

Acknowledgments

The authors would like to acknowledge the assistance of the Center for Advanced Microscopy and the Nikon Imaging Center at the Feinberg School of Medicine, Northwestern University, for assistance with imaging and the use of the Nikon N-SIM Microscope.

Additional Information

Funding

The Nikon N-SIM used in this study was purchased through the support of NIH 1S10OD016342-01. The authors acknowledge the National Cancer Institute (T32CA080621 for M.K.), Japan Society for Promoting Science (JSPS, grant 18H06045 for T.S.), Swiss National Science Foundation Grant (SNSF 31003A_179418 to O.M), and the National Institute of General Medical Sciences (R35GM119619 to K.J; R01GM106023 to Y.Z. and R.D.G).

Author Contributions

MK, TS, SA, and RDG conceived of the study. TS and MK performed the light microscopy experiments. MT and OM analyzed Cryo-ET data. MK and SA ran the Western blots. JRT and YZ provided lamin null cell lines. MK and KJ performed the image and statistical analysis. MK, TS, and MT prepared the figures. All authors contributed to the writing of the paper.

Author ORCIDs

- Mark Kittisopikul https://orcid.org/0000-0002-9558-6248
- Takeshi Shimi https://orcid.org/0000-0002-9864-1820
- Joseph R. Tran https://orcid.org/0000-0002-7467-8995
- Yixian Zheng https://orcid.org/0000-0002-1992-4014
- Ohad Medalia https://orcid.org/0000-0003-0994-2937
- Khuloud Jaqaman http://orcid.org/0000-0003-3471-1911
- Stephen A. Adam https://orcid.org/0000-0003-3444-7655
- Robert D. Goldman http://orcid.org/0000-0003-0383-1435

References

Aebi U, Cohn J, Buhle L, Gerace L. The nuclear lamina is a meshwork of intermediate-type filaments. Nature. 1986 oct; 323(6088):560–564. https://doi.org/10.1038%2F323560a0, doi: 10.1038/323560a0.

Al-Haboubi T, Shumaker DK, Köser J, Wehnert M, Fahrenkrog B. Distinct association of the nuclear pore protein Nup153 with A- and B-type lamins. Nucleus. 2011 sep; 2(5):500–509. https://doi.org/10.4161%2Fnucl.2.5.17913, doi: 10.4161/nucl.2.5.17913.

Beck M, Hurt E. The nuclear pore complex: understanding its function through structural insight. Nature Reviews Molecular Cell Biology. 2016 dec; 18(2):73–89. https://doi.org/10.1038%2Fnrm.2016.147, doi: 10.1038/nrm.2016.147.

Biamonti G, Giacca M, Perini G, Contreas G, Zentilin L, Weighardt F, Guerra M, Valle GD, Saccone S, Riva S. The gene for a novel human lamin maps at a highly transcribed locus of chromosome 19 which replicates at the onset of S-phase. Molecular and Cellular Biology. 1992 aug; 12(8):3499–3506. https://doi.org/10.1128%2Fmcb.12.8.3499, doi: 10.1128/mcb.12.8.3499.

Broers JL, Machiels BM, van Eys GJ, Kuijpers HJ, Manders EM, van Driel R, Ramaekers FC. Dynamics of the nuclear lamina as monitored by GFP-tagged A-type lamins. Journal of Cell Science. 1999; 112(20):3463–3475. https://jcs.biologists.org/content/112/20/3463.

Dechat T, Shimi T, Adam SA, Rusinol AE, Andres DA, Spielmann HP, Sinensky MS, Goldman RD. Alterations in mitosis and cell cycle progression caused by a mutant lamin A known to accelerate human aging. Proceedings of the National Academy of Sciences. 2007 Mar; 104(12):4955–4960. https://doi.org/10.1073/pnas.0700854104, doi: 10.1073/pnas.0700854104.

Dessev G, Iovcheva-Dessev C, Bischoff JR, Beach D, Goldman R. A complex containing p34cdc2 and cyclin B phosphorylates the nuclear lamin and disassembles nuclei of clam oocytes in vitro. The Journal of Cell Biology. 1991 feb; 112(4):523–533. https://doi.org/10.1083%2Fjcb.112.4.523, doi: 10.1083/jcb.112.4.523.

Doucet CM, Talamas JA, Hetzer MW. Cell Cycle-Dependent Differences in Nuclear Pore Complex Assembly in Metazoa. Cell. 2010 jun; 141(6):1030–1041. https://doi.org/10.1016%2Fj.cell.2010.04.036, doi: 10.1016/j.cell.2010.04.036.

619 **Duheron V**, Chatel G, Sauder U, Oliveri V, Fahrenkrog B. Structural characterization of altered nucleoporin
620 Nup153 expression in human cells by thin-section electron microscopy. Nucleus. 2014 nov; 5(6):601–612.
621 https://doi.org/10.4161%2F19491034.2014.990853, doi: 10.4161/19491034.2014.990853.

622 **Dwyer N**, Blobel G. A modified procedure for the isolation of a pore complex-lamina fraction from rat liver
623 nuclei. The Journal of Cell Biology. 1976 sep; 70(3):581–591. https://doi.org/10.1083%2Fjcb.70.3.581, doi:
624 10.1083/jcb.70.3.581.

625 **Favreau C**, Worman HJ, Wozniak RW, Frappier T, Courvalin JC. Cell Cycle-Dependent Phosphorylation of
626 Nucleoporins and Nuclear Pore Membrane Protein Gp210†. Biochemistry. 1996 jan; 35(24):8035–8044.
627 https://doi.org/10.1021%2Fbi9600660, doi: 10.1021/bi9600660.

628 **Fawcett DW**. On the occurrence of a fibrous lamina on the inner aspect of the nuclear envelope in certain
629 cells of vertebrates. American Journal of Anatomy. 1966 jul; 119(1):129–145. https://doi.org/10.1002%2Faja.
630 1001190108, doi: 10.1002/aja.1001190108.

631 **Fisher DZ**, Chaudhary N, Blobel G. cDNA sequencing of nuclear lamins A and C reveals primary and secondary
632 structural homology to intermediate filament proteins. Proceedings of the National Academy of Sciences.
633 1986 sep; 83(17):6450–6454. https://doi.org/10.1073%2Fpnas.83.17.6450, doi: 10.1073/pnas.83.17.6450.

634 **Foisner R**, Gerace L. Integral membrane proteins of the nuclear envelope interact with lamins and chro-
635 mosomes, and binding is modulated by mitotic phosphorylation. Cell. 1993 jul; 73(7):1267–1279. https:
636 //doi.org/10.1016%2F0092-8674%2893%2990355-t, doi: 10.1016/0092-8674(93)90355-t.

637 **Franz C**, Walczak R, Yavuz S, Santarella R, Gentzel M, Askjaer P, Galy V, Hetzer M, Mattaj IW, Antonin W. MEL-
638 28/ELYS is required for the recruitment of nucleoporins to chromatin and postmitotic nuclear pore com-
639 plex assembly. EMBO reports. 2007 jan; 8(2):165–172. https://doi.org/10.1038%2Fsj.embor.7400889, doi:
640 10.1038/sj.embor.7400889.

641 **Gerace L**, Blobel G. The nuclear envelope lamina is reversibly depolymerized during mitosis. Cell. 1980 jan;
642 19(1):277–287. https://doi.org/10.1016%2F0092-8674%2880%2990409-2, doi: 10.1016/0092-8674(80)90409-2.

643 **Goldman AE**, Maul G, Steinert PM, Yang HY, Goldman RD. Keratin-like proteins that coisolate with intermediate
644 filaments of BHK-21 cells are nuclear lamins. Proceedings of the National Academy of Sciences. 1986 jun;
645 83(11):3839–3843. https://doi.org/10.1073%2Fpnas.83.11.3839, doi: 10.1073/pnas.83.11.3839.

646 **Goldman RD**, Shumaker DK, Erdos MR, Eriksson M, Goldman AE, Gordon LB, Gruenbaum Y, Khuon S, Mendez
647 M, Varga R, Collins FS. Accumulation of mutant lamin A causes progressive changes in nuclear architec-
648 ture in Hutchinson–Gilford progeria syndrome. Proceedings of the National Academy of Sciences. 2004 jun;
649 101(24):8963–8968. https://doi.org/10.1073%2Fpnas.0402943101, doi: 10.1073/pnas.0402943101.

650 **Guelen L**, Pagie L, Brasset E, Meuleman W, Faza MB, Talhout W, Eussen BH, de Klein A, Wessels L, de Laat
651 W, van Steensel B. Domain organization of human chromosomes revealed by mapping of nuclear lamina
652 interactions. Nature. 2008 may; 453(7197):948–951. https://doi.org/10.1038%2Fnature06947, doi: 10.1038/na-
653 ture06947.

654 **Guo Y**, Zheng Y. Lamins position the nuclear pores and centrosomes by modulating dynein. Molecular Biology
655 of the Cell. 2015 oct; 26(19):3379–3389. https://doi.org/10.1091%2Fmbc.e15-07-0482, doi: 10.1091/mbc.e15-
656 07-0482.

657 **Hase ME**, Cordes VC. Direct Interaction with Nup153 Mediates Binding of Tpr to the Periphery of the Nuclear
658 Pore Complex. Molecular Biology of the Cell. 2003 may; 14(5):1923–1940. https://doi.org/10.1091%2Fmbc.
659 e02-09-0620, doi: 10.1091/mbc.e02-09-0620.

660 **Höger TH**, Zatloukal K, Waizenegger I, Krohne G. Characterization of a second highly conserved B-type lamin
661 present in cells previously thought to contain only a single B-type lamin. Chromosoma. 1990 oct; 99(6):379–
662 390. https://doi.org/10.1007%2Fbf01726689, doi: 10.1007/bf01726689.

663 **Ibarra A**, Hetzer MW. Nuclear pore proteins and the control of genome functions. Genes & Development. 2015
664 feb; 29(4):337–349. https://doi.org/10.1101%2Fgad.256495.114, doi: 10.1101/gad.256495.114.

665 **Kay RR**, Fraser D, Johnston IR. A Method for the Rapid Isolation of Nuclear Membranes from Rat Liver. Charac-
666 terisation of the Membrane Preparation and Its Associated DNA Polymerase. European Journal of Biochem-
667 istry. 1972 oct; 30(1):145–154. https://doi.org/10.1111%2Fj.1432-1033.1972.tb02081.x, doi: 10.1111/j.1432-
668 1033.1972.tb02081.x.

669 **Kim Y**, Sharov AA, McDole K, Cheng M, Hao H, Fan CM, Gaiano N, Ko MSH, Zheng Y. Mouse B-Type Lamins Are
670 Required for Proper Organogenesis But Not by Embryonic Stem Cells. Science. 2011 nov; 334(6063):1706–
671 1710. https://doi.org/10.1126%2Fscience.1211222, doi: 10.1126/science.1211222.

672 **Kim Y**, Zheng Y. Generation and characterization of a conditional deletion allele for Lmna in mice. Biochemical
673 and Biophysical Research Communications. 2013 Oct; 440(1):8–13. https://doi.org/10.1016/j.bbrc.2013.08.082,
674 doi: 10.1016/j.bbrc.2013.08.082.

675 **Kittisopikul M**, Vahabikashi A, Shimi T, Goldman RD, Jaqaman K. Adaptive-Resolution Multi-Orientation
676 Analysis of Complex Filamentous Network Images. . 2019 sep; https://doi.org/10.1101%2F757005, doi:
677 10.1101/757005.

678 **Kochin V**, Shimi T, Torvaldson E, Adam SA, Goldman A, Pack CG, Melo-Cardenas J, Imanishi SY, Goldman RD,
679 Eriksson JE. Interphase phosphorylation of lamin A. Journal of Cell Science. 2014 apr; 127(12):2683–2696.
680 https://doi.org/10.1242%2Fjcs.141820, doi: 10.1242/jcs.141820.

681 **Krull S**, Thyberg J, Björkroth B, Rackwitz HR, Cordes VC. Nucleoporins as Components of the Nuclear Pore
682 Complex Core Structure and Tpr as the Architectural Element of the Nuclear Basket. Molecular Biology of
683 the Cell. 2004 sep; 15(9):4261–4277. https://doi.org/10.1091%2Fmbc.e04-03-0165, doi: 10.1091/mbc.e04-03-
684 0165.

685 **Lin F**, Worman HJ. Structural organization of the human gene encoding nuclear lamin A and nuclear lamin
686 C. Journal of Biological Chemistry. 1993; 268(22):16321–16326. http://www.jbc.org/content/268/22/16321.
687 abstract.

688 **Lin F**, Worman HJ. Structural Organization of the Human Gene (LMNB1) Encoding Nuclear Lamin B1. Genomics.
689 1995 may; 27(2):230–236. https://doi.org/10.1006%2Fgeno.1995.1036, doi: 10.1006/geno.1995.1036.

690 **Linkert M**, Rueden CT, Allan C, Burel JM, Moore W, Patterson A, Loranger B, Moore J, Neves C, MacDonald D,
691 Tarkowska A, Sticco C, Hill E, Rossner M, Eliceiri KW, Swedlow JR. Metadata matters: access to image data in
692 the real world. The Journal of Cell Biology. 2010 May; 189(5):777–782. https://doi.org/10.1083/jcb.201004104,
693 doi: 10.1083/jcb.201004104.

694 **Macaulay C**, Meier E, Forbes DJ. Differential Mitotic Phosphorylation of Proteins of the Nuclear Pore Com-
695 plex. Journal of Biological Chemistry. 1995 jan; 270(1):254–262. https://doi.org/10.1074%2Fjbc.270.1.254, doi:
696 10.1074/jbc.270.1.254.

697 **Maeno H**, Sugimoto K, Nakajima N. Genomic Structure of the Mouse Gene (Lmnb1) Encoding Nu-
698 clear Lamin B1. Genomics. 1995 nov; 30(2):342–346. https://doi.org/10.1006%2Fgeno.1995.9868, doi:
699 10.1006/geno.1995.9868.

700 **Maul G**. Studies in ultrastructure. International review of cytology : Supplement ; 6, New York: Academic Press;
701 1977.

702 **McCloskey A**, Ibarra A, Hetzer MW. Tpr regulates the total number of nuclear pore complexes per cell nu-
703 cleus. Genes & Development. 2018 sep; 32(19-20):1321–1331. https://doi.org/10.1101%2Fgad.315523.118,
704 doi: 10.1101/gad.315523.118.

705 **McKeon FD**, Kirschner MW, Caput D. Homologies in both primary and secondary structure between nuclear
706 envelope and intermediate filament proteins. Nature. 1986 feb; 319(6053):463–468. https://doi.org/10.1038%
707 2F319463a0, doi: 10.1038/319463a0.

708 **Moir RD**, Yoon M, Khuon S, Goldman RD. Nuclear Lamins a and B1. The Journal of Cell Biology. 2000 dec;
709 151(6):1155–1168. https://doi.org/10.1083%2Fjcb.151.6.1155, doi: 10.1083/jcb.151.6.1155.

710 **Nickell S**, Förster F, Linaroudis A, Net WD, Beck F, Hegerl R, Baumeister W, Plitzko JM. TOM software toolbox:
711 acquisition and analysis for electron tomography. Journal of Structural Biology. 2005 Mar; 149(3):227–234.
712 https://doi.org/10.1016/j.jsb.2004.10.006, doi: 10.1016/j.jsb.2004.10.006.

713 **Ou HD**, Phan S, Deerinck TJ, Thor A, Ellisman MH, O'Shea CC. ChromEMT: Visualizing 3D chromatin structure
714 and compaction in interphase and mitotic cells. Science. 2017 jul; 357(6349):eaag0025. https://doi.org/10.
715 1126%2Fscience.aag0025, doi: 10.1126/science.aag0025.

716 **Peric-Hupkes D**, Meuleman W, Pagie L, Bruggeman SWM, Solovei I, Brugman W, Gräf S, Flicek P, Kerkhoven RM,
717 van Lohuizen M, Reinders M, Wessels L, van Steensel B. Molecular Maps of the Reorganization of Genome-
718 Nuclear Lamina Interactions during Differentiation. Molecular Cell. 2010 may; 38(4):603–613. https://doi.
719 org/10.1016%2Fj.molcel.2010.03.016, doi: 10.1016/j.molcel.2010.03.016.

720 **Peter M**, Nakagawa J, Dorée M, Labbé JC, Nigg EA. In vitro disassembly of the nuclear lamina and M phase-
721 specific phosphorylation of lamins by cdc2 kinase. Cell. 1990 may; 61(4):591–602. https://doi.org/10.1016%
722 2F0092-8674%2890%2990471-p, doi: 10.1016/0092-8674(90)90471-p.

723 **Rabut G**, Doye V, Ellenberg J. Mapping the dynamic organization of the nuclear pore complex inside sin-
724 gle living cells. Nature Cell Biology. 2004 oct; 6(11):1114–1121. https://doi.org/10.1038%2Fncb1184, doi:
725 10.1038/ncb1184.

726 **Rasala BA**, Orjalo AV, Shen Z, Briggs S, Forbes DJ. ELYS is a dual nucleoporin/kinetochore protein required for
727 nuclear pore assembly and proper cell division. Proceedings of the National Academy of Sciences. 2006 nov;
728 103(47):17801–17806. https://doi.org/10.1073%2Fpnas.0608484103, doi: 10.1073/pnas.0608484103.

729 **Rasala BA**, Ramos C, Harel A, Forbes DJ. Capture of AT-rich Chromatin by ELYS Recruits POM121 and NDC1 to
730 Initiate Nuclear Pore Assembly. Molecular Biology of the Cell. 2008 sep; 19(9):3982–3996. https://doi.org/10.
731 1091%2Fmbc.e08-01-0012, doi: 10.1091/mbc.e08-01-0012.

732 **Roux KJ**, Kim DI, Raida M, Burke B. A promiscuous biotin ligase fusion protein identifies proximal and interacting
733 proteins in mammalian cells. Journal of Cell Biology. 2012 mar; 196(6):801–810. https://doi.org/10.1083%
734 2Fjcb.201112098, doi: 10.1083/jcb.201112098.

735 **Scheer U**, Kartenbeck J, Trendelenburg MF, Stadler J, Franke WW. Experimental disintegration of the nuclear
736 envelope. Evidence for pore-connecting fibrils. The Journal of Cell Biology. 1976 apr; 69(1):1–18. https://doi.
737 org/10.1083%2Fjcb.69.1.1, doi: 10.1083/jcb.69.1.1.

738 **Shimi T**, Kittisopikul M, Tran J, Goldman AE, Adam SA, Zheng Y, Jaqaman K, Goldman RD. Structural organization
739 of nuclear lamins A, C, B1, and B2 revealed by superresolution microscopy. Molecular Biology of the Cell.
740 2015 nov; 26(22):4075–4086. https://doi.org/10.1091%2Fmbc.e15-07-0461, doi: 10.1091/mbc.e15-07-0461.

741 **Stelzer**. Contrast, resolution, pixelation, dynamic range and signal-to-noise ratio: fundamental limits to reso-
742 lution in fluorescence light microscopy. Journal of Microscopy. 1998 Jan; 189(1):15–24. https://doi.org/10.
743 1046/j.1365-2818.1998.00290.x, doi: 10.1046/j.1365-2818.1998.00290.x.

744 **Sullivan T**, Escalante-Alcalde D, Bhatt H, Anver M, Bhat N, Nagashima K, Stewart CL, Burke B. Loss of a-Type
745 Lamin Expression Compromises Nuclear Envelope Integrity Leading to Muscular Dystrophy. The Journal of
746 Cell Biology. 1999 nov; 147(5):913–920. https://doi.org/10.1083%2Fjcb.147.5.913, doi: 10.1083/jcb.147.5.913.

747 **Tatli M**, Medalia O. Insight into the functional organization of nuclear lamins in health and disease.
748 Current Opinion in Cell Biology. 2018 oct; 54:72–79. https://doi.org/10.1016%2Fj.ceb.2018.05.001, doi:
749 10.1016/j.ceb.2018.05.001.

750 **Toda T**, Hsu JY, Linker SB, Hu L, Schafer ST, Mertens J, Jacinto FV, Hetzer MW, Gage FH. Nup153 Interacts with
751 Sox2 to Enable Bimodal Gene Regulation and Maintenance of Neural Progenitor Cells. Cell Stem Cell. 2017
752 nov; 21(5):618–634.e7. https://doi.org/10.1016%2Fj.stem.2017.08.012, doi: 10.1016/j.stem.2017.08.012.

753 **Turgay Y**, Eibauer M, Goldman AE, Shimi T, Khayat M, Ben-Harush K, Dubrovsky-Gaupp A, Sapra KT, Goldman
754 RD, Medalia O. The molecular architecture of lamins in somatic cells. Nature. 2017 mar; 543(7644):261–264.
755 https://doi.org/10.1038%2Fnature21382, doi: 10.1038/nature21382.

756 **Unser M**. Splines: a perfect fit for signal and image processing. IEEE Signal Processing Magazine. 1999; 16(6):22–
757 38. https://doi.org/10.1109/79.799930, doi: 10.1109/79.799930.

758 **Vergnes L**, Peterfy M, Bergo MO, Young SG, Reue K. Lamin B1 is required for mouse development and nuclear
759 integrity. Proceedings of the National Academy of Sciences. 2004 jul; 101(28):10428–10433. https://doi.org/
760 10.1073%2Fpnas.0401424101, doi: 10.1073/pnas.0401424101.

761 **Walther TC**. The nucleoporin Nup153 is required for nuclear pore basket formation, nuclear pore complex
762 anchoring and import of a subset of nuclear proteins. The EMBO Journal. 2001 oct; 20(20):5703–5714. https:
763 //doi.org/10.1093%2Femboj%2F20.20.5703, doi: 10.1093/emboj/20.20.5703.

764 **Xie W**, Chojnowski A, Boudier T, Lim JSY, Ahmed S, Ser Z, Stewart C, Burke B. A-type Lamins Form Distinct
765 Filamentous Networks with Differential Nuclear Pore Complex Associations. Current Biology. 2016 oct;
766 26(19):2651–2658. https://doi.org/10.1016%2Fj.cub.2016.07.049, doi: 10.1016/j.cub.2016.07.049.

Appendix 1

Localization of Lamin Fibers in Orientation Space

In order to localize lamin fibers, we use an image analysis algorithm that we previously developed that involves the construction of a three dimensional orientation space by augmenting a 2-D image with orientation as an additional third dimension ***Kittisopikul et al.*** (***2019***). There we focused on addressing the continuous nature of the orientation dimension, we leave the spatial dimensions discretely sampled and localize line detections to nearest pixel in the Non-Maximum Suppression (NMS) and Non-Local Maxima Suppression (NLMS) procedures.

Here we extend the procedure by using the orientations to localize lines, the lamin fibers, to sub-pixel precision by also treating the spatial dimensions as continuous. Given sufficient signal-to-noise ratios and sampling in excess of that required by the Nyquist-Shannon-Whittaker-Kotelnikov sampling theorem, the spatial dimension could also be treated continuously through interpolation. In particular, we use spline interpolation (***Unser, 1999***). In that case, we can state the localization problem as solving a system of partial differential equations where $R(x, y, \theta; K)$ is the steerable filter response at some location (x, y) at orientation θ at the orientation-resolution K.

$$\text{For } \vec{v} = (\cos(\phi), \sin(\phi)), \text{ we want all } (x, y, \phi) \text{ such that}$$

$$\frac{\partial R(x, y, \phi; K_1)}{\partial \phi} = 0, \quad \frac{\partial^2 R(x, y, \phi; K_1)}{\partial \phi^2} < 0$$

$$\frac{\partial R(x, y, \phi; K_2)}{\partial \vec{v}} = 0 = \frac{\partial R(x, y, \phi; K_2)}{\partial x} \cos(\phi) + \frac{\partial R(x, y, \phi; K_2)}{\partial y} \sin(\phi)$$

$$\frac{\partial^2 R(x, y, \phi; K_2)}{\partial \vec{v}^2} < 0$$

$\vec{v}$ is a vector normal to the structure being localized. As explained in ***Kittisopikul et al.*** (***2019***), K_1 and K_2 may differ since the orientation resolution used for orientation detection may differ from the orientation resolution used to localize the detection in space.

Localization of Lamin Meshwork Face Centers

To understand the relationship of NPCs to the lamin structure, we also measured the distance of the NPCs from their "centers" which we defined as the points furthest away from the lamins within a local neighborhood.

Face centers were localized by identifying local maxima of the distance transform relative to the lamin fibers. A 2D disc with a five pixel radius (150 nm) was used as a structuring element with morphological dilation. This identified the maximum distance within a disc centered at each pixel. The local maxima were detected at the points when the maximum distance within the disc coincided with an identical distance assigned to that pixel via the distance transform. If a connected region with points equidistant from the lamin fibers were found, the centroid of that region was selected as the face center.

Because faces are not always convex or there maybe lamin fibers protruding into faces, multiple distinct centers may be detected. In this case, the distance from the NPC is measured to the nearest face center.

Table 1A: Lamin Fiber$_{8\sigma4}$NPC Center to Center Distance Distributions

Cell Genotype	Lamin Labeled	Observed (nm) Median	St. Dev.	Expected (nm) Median	St. Dev.	Obs. - Exp. (nm) Median	St. Dev.	P-Values Median	St. Dev.	Num. of NPCs N
wt	**LA**	40.4	38.0	33.5	56.5	6.9	-18.5	0.00		14780
wt	**LC**	32.8	35.0	32.1	49.4	0.7	-14.5	0.37	0.01	11459
wt	**LB1**	38.1	36.2	32.1	56.9	6.0	-20.7	0.00		15150
wt	**LB2**	27.6	29.2	28.1	38.7	-0.6	-9.6	0.00		17146
Lmnb1-/-	**LA**	45.1	48.6	42.4	216.8	2.7	-168.2	0.59	0.00	11971
Lmna-/-	**LB1**	34.9	34.5	35.8	297.7	-0.8	-263.1	0.00		9740

Caption: Median and standard deviation of the observed and expected lamin fiber to NPC center to center distances, the difference between them, p-values (see Methods), and number of NPCs

Table 1B: Face - NPC Center to Center Distance Distributions

Cell Genotype	Lamin Labeled	Observed (nm) Median	St. Dev.	Expected (nm) Median	St. Dev.	Obs. - Exp. (nm) Median	St. Dev.	P-Values Median	St. Dev.	Num. of NPCs N
wt	**LA**	119.3	62.6	130.9	78.3	-11.7	-15.7	0.00		14780
wt	**LC**	122.4	57.1	125.7	69.0	-3.3	-11.9	0.00		11459
wt	**LB1**	118.3	56.8	129.1	76.0	-10.8	-19.2	0.00		15150
wt	**LB2**	116.7	51.5	117.3	58.9	-0.6	-7.3	0.25	0.08	17146
Lmnb1-/-	**LA**	124.0	90.0	146.0	235.2	-22.0	-145.2	0.00		11971
Lmna-/-	**LB1**	122.1	55.7	133.2	304.3	-11.1	-248.6	0.00		9740

Caption: Median and standard deviation of the observed and expected lamin face to NPC distances, the difference between them, p-values (see Methods), and number of NPCs.

Table 2A: Lamin Fiber to NPC Center to Center Distance Distributions

siRNA Knockdown	Lamin Labeled	Observed (nm) Median	Observed (nm) St. Dev.	Expected (nm) Median	Expected (nm) St. Dev.	Obs. - Exp. (nm) Median	Obs. - Exp. (nm) St. Dev.	P vs Exp. Median	P vs Exp. St. Dev.	Obs. - Scram. Median (nm)	P vs Scram. Median	Num. of NPCs N
Scrambled	LA	50.9	39.5	33.6	40.4	17.3	-0.9	0.00				39096
TPR KD	LA	59.0	39.5	31.9	36.9	27.1	2.6	0.00		8.2	0.00	40767
NUP153 KD	LA	50.1	38.6	31.1	35.7	19.0	2.8	0.00		-0.8	0.00	36066
ELYS KD	LA	70.8	48.9	32.9	42.4	37.9	6.5	0.00		20.0	0.00	21521
Scrambled	LC	42.9	36.1	31.7	42.6	11.2	-6.5	0.00				37760
TPR KD	LC	56.6	38.1	31.2	54.4	25.4	-16.2	0.00		13.7	0.00	35489
NUP153 KD	LC	39.9	35.1	29.8	35.6	10.1	-0.5	0.00		-3.0	0.00	39988
ELYS KD	LC	63.1	46.7	32.8	44.2	30.3	2.6	0.00		20.2	0.00	27053
Scrambled	LB1	51.6	42.4	35.4	51.8	16.2	-9.4	0.00				37383
TPR KD	LB1	52.1	38.4	31.3	49.0	20.8	-10.6	0.00		0.5	0.00	40899
NUP153 KD	LB1	46.9	41.3	35.2	40.6	11.7	0.7	0.00		-4.7	0.00	31145
ELYS KD	LB1	48.5	40.1	31.1	40.6	17.4	-0.5	0.00		-3.1	0.00	24981
Scrambled	LB2	30.1	33.8	34.4	67.2	-4.4	-33.4	0.00				35444
TPR KD	LB2	28.6	30.3	30.2	75.0	-1.7	-44.7	0.00		-1.5	0.00	36974
NUP153 KD	LB2	25.6	30.9	32.3	39.9	-6.6	-9.0	0.00		-4.4	0.00	31628
ELYS KD	LB2	34.2	33.8	31.2	40.2	3.0	-6.3	0.00		4.1	0.00	25215

Caption: Median and standard deviation of the observed and expected lamin fiber to NPC center to center distances, the difference between them, p-values (see Methods), and number of NPCs. The distributions were also comapared to scrambled siRNA control.

Table 2B: Lamin Face to NPC Center to Center Distance Distributions

siRNA Knockdown	Lamin Labeled	Observed (nm) Median	Observed (nm) St. Dev.	Expected (nm) Median	Expected (nm) St. Dev.	Obs. - Exp. (nm) Median	Obs. - Exp. (nm) St. Dev.	P vs Exp. Median	P vs Exp. St. Dev.	Obs. - Scram. Median (nm)	P vs Scram. Median	Num. of NPCs N
Scrambled	LA	106.2	60.6	132.0	63.6	-25.8	-3.0	0.00		0.0	1.00	39096
TPR KD	LA	90.0	58.0	127.1	60.0	-37.1	-2.0	0.00		-16.2	0.00	40767
NUP153 KD	LA	99.7	57.0	126.2	58.0	-26.6	-1.1	0.00		-6.5	0.00	36066
ELYS KD	LA	89.7	58.8	129.7	64.4	-39.9	-5.6	0.00		-16.4	0.00	21521
Scrambled	LC	109.1	58.1	126.5	65.2	-17.4	-7.2	0.00		0.0	1.00	37760
TPR KD	LC	89.9	55.6	125.8	73.4	-35.9	-17.7	0.00		-19.2	0.00	35489
NUP153 KD	LC	106.6	55.5	122.9	57.7	-16.3	-2.2	0.00		-2.5	0.00	39988
ELYS KD	LC	96.1	59.3	129.9	65.9	-33.7	-6.6	0.00		-13.0	0.00	27053
Scrambled	LB1	114.0	63.4	138.6	73.4	-24.6	-9.9	0.00		0.0	1.00	37383
TPR KD	LB1	96.7	56.9	126.6	68.4	-30.0	-11.4	0.00		-17.3	0.00	40899
NUP153 KD	LB1	118.8	63.7	135.8	65.7	-17.0	-2.0	0.00		4.8	0.00	31145
ELYS KD	LB1	101.5	58.2	125.6	62.2	-24.1	-4.0	0.00		-12.5	0.00	24981
Scrambled	LB2	138.8	59.7	134.6	85.8	4.2	-26.1	0.00		0.0	1.00	35444
TPR KD	LB2	125.2	54.8	124.1	90.0	1.1	-35.1	0.00		-13.6	0.00	36974
NUP153 KD	LB2	139.7	60.4	129.1	64.1	10.6	-3.7	0.00		0.9	0.00	31628
ELYS KD	LB2	120.6	56.4	126.5	62.4	-5.9	-6.0	0.00		-18.2	0.00	25215

Caption: Median and standard deviation of the observed and expected lamin face to NPC distances, the difference between them, p-values (see Methods), and number of NPCs. The distributions were also comapared to scrambled siRNA control.

Table 2C: Face Radii Distributions (Fiber to NPC + Face to NPC)

siRNA Knockdown	Lamin Labeled	Observed (nm) Median	Observed (nm) St. Dev.	Expected (nm) Median	Expected (nm) St. Dev.	Obs. - Exp. (nm) Median	Obs. - Exp. (nm) St. Dev.	P vs Exp. Median	P vs Exp. St. Dev.	Obs. - Scram. Median (nm)	P vs Scram. Median	Num. of NPCs N
Scrambled	LA	163.3	53.2	171.9	67.4	-8.6	-14.2	0.00				39096
TPR KD	LA	154.3	49.6	164.3	59.9	-10.0	-10.4	0.00		-9.1	0.00	40767
NUP153 KD	LA	155.9	48.3	162.8	56.6	-6.9	-8.3	0.00		-7.5	0.00	36066
ELYS KD	LA	169.7	50.9	168.9	72.3	0.8	-21.3	0.38	0.00	6.3	0.00	21521
Scrambled	LC	157.0	50.8	163.3	77.4	-6.4	-26.6	0.00				37760
TPR KD	LC	150.8	47.0	161.5	103.3	-10.7	-56.2	0.00		-6.2	0.00	35489
NUP153 KD	LC	152.8	47.3	157.8	58.9	-4.9	-11.7	0.00		-4.1	0.00	39988
ELYS KD	LC	167.5	52.0	169.0	77.1	-1.5	-25.1	0.00		10.5	0.00	27053
Scrambled	LB1	174.7	54.7	181.8	92.2	-7.1	-37.5	0.00				37383
TPR KD	LB1	154.4	48.0	163.2	89.4	-8.9	-41.4	0.00		-20.3	0.00	40899
NUP153 KD	LB1	173.6	56.1	178.1	67.1	-4.4	-11.0	0.00		-1.1	0.06	31145
ELYS KD	LB1	157.1	48.8	162.1	70.6	-5.0	-21.7	0.00		-17.6	0.00	24981
Scrambled	LB2	175.5	52.5	175.0	129.5	0.4	-76.9	0.22	0.95			35444
TPR KD	LB2	159.0	47.7	158.7	147.2	0.3	-99.4	0.16	0.40	-16.4	0.00	36974
NUP153 KD	LB2	170.6	55.2	166.5	68.9	4.0	-13.7	0.00		-4.9	0.00	31628
ELYS KD	LB2	160.7	48.7	162.7	70.3	-2.0	-21.6	0.00		-14.8	0.00	25215

Caption: Median and standard deviation of the observed and expected sum of lamin fiber and lamin face to NPC distances, the difference between them, p-values (see Methods), and number of NPCs. The distributions were also comapared to scrambled siRNA control.

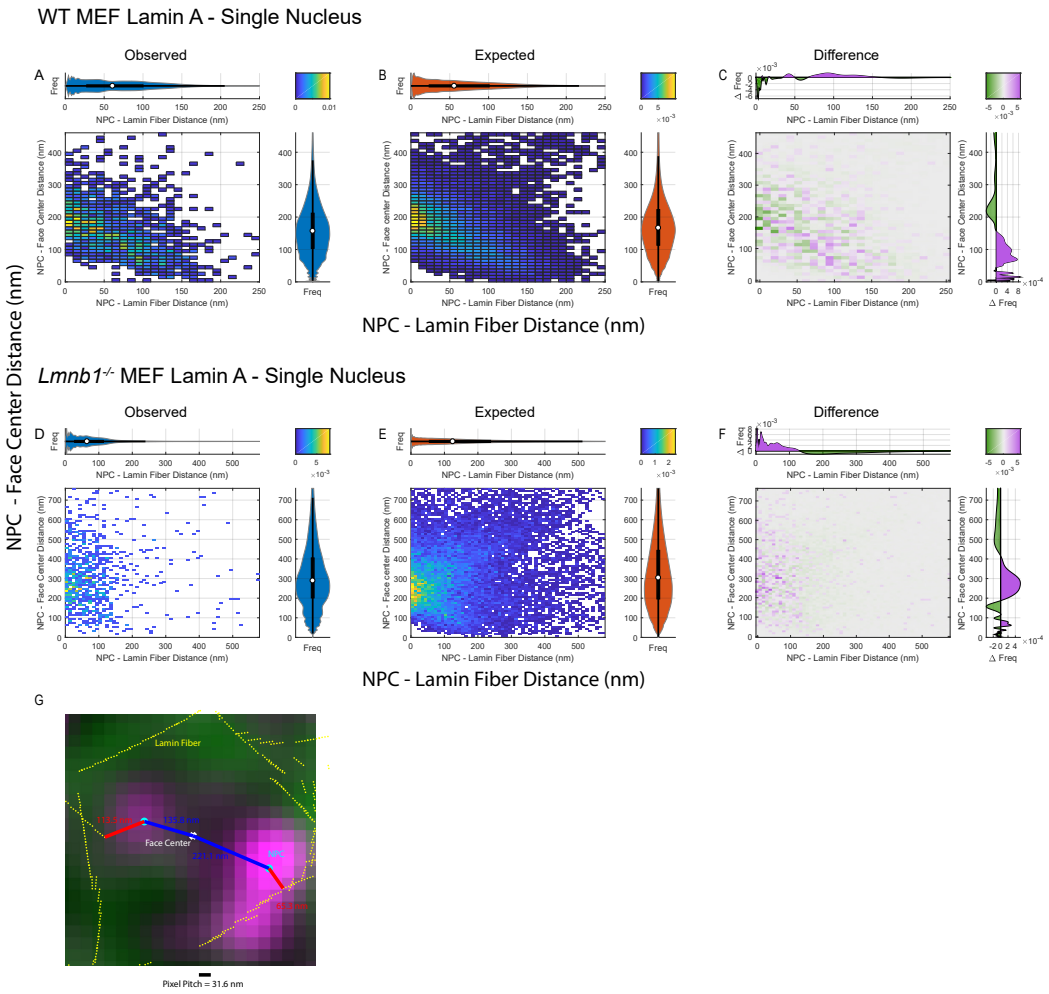

806

Legend A) Observed bivariate histogram of NPC to LA face center distances versus NPC to lamin A fiber distances of a single WT MEF Lamin A nucleus shown in panel A of the main figure. B) Expected bivariate histogram of NPC to lamin A face center distances versus NPC to lamin A fiber distances of a single WT MEF Lamin A nucleus under the null hypothesis. C) Difference between the observed and expected distance distributions with purple indicating where the observed exceeds the expected frequency and green showing when the observed frequency is less than the expected frequency. D-F) Same as A-C except for the single Lmnb1-/- nucleus shown in panel A of the main figure. Marginal violin plots and box plots of the distances correspond with the half-violin plot counterparts of the same orientation and color as in Panel B of the main figure. G) Zoomed in plot showing the NPC to lamin A fiber (red) and NPC to lamin A face center distances (blued) measured. Other colors correspond with those as in panel B of the main figure.

Figure 2–Figure supplement 1. Bivariate histograms of LA Fiber-NPC and Face Center-NPC Distances in Single Nuclei. Illustration of Distances.

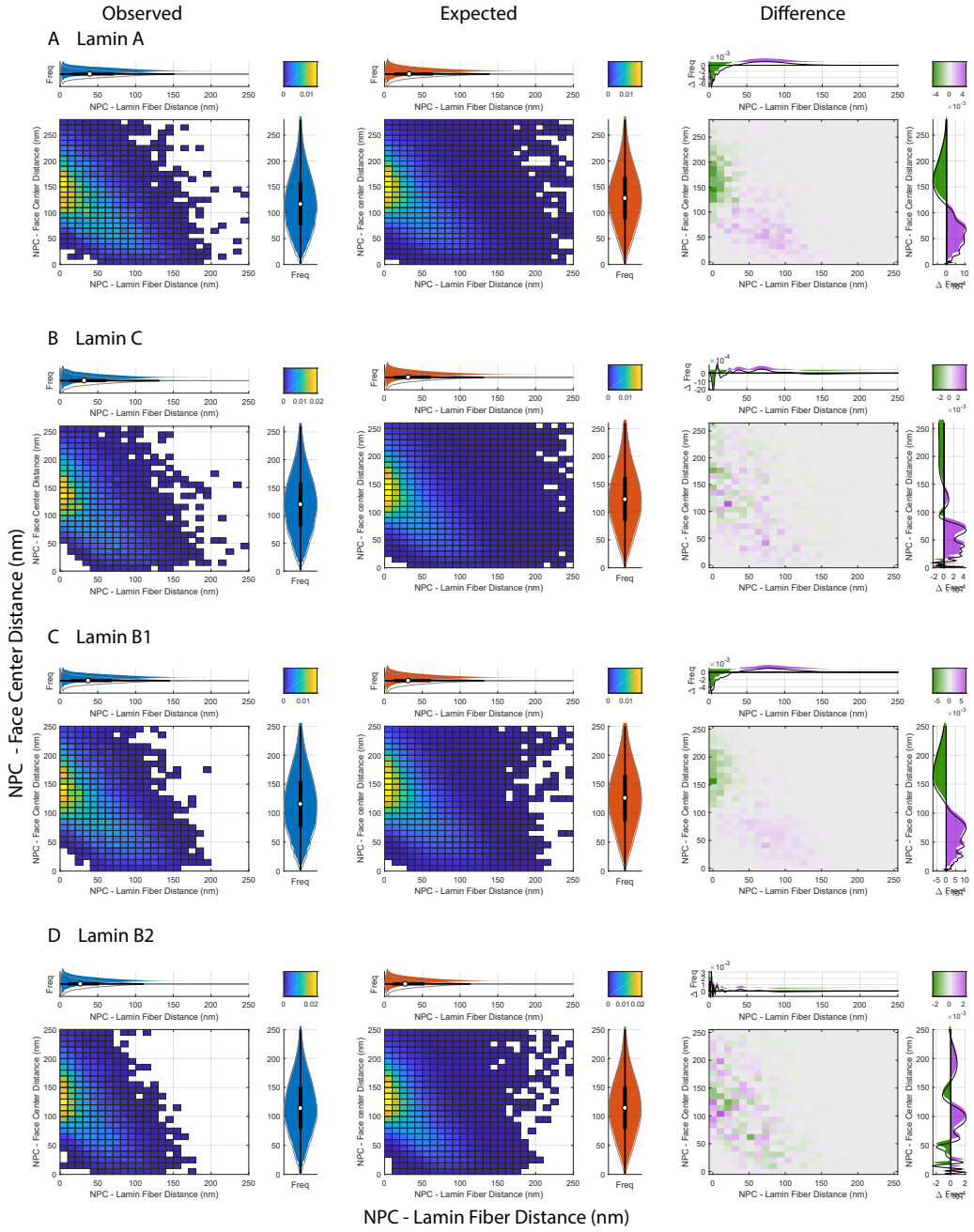

Legend A) First row shows a bivariate distribution of NPC to Lamin A fiber and face center distances in WT MEFs. B) Second row shows bivariate distributions of NPC to Lamin C fiber and face center distances. C) Third row shows bivariate distributions of NPC to Lamin B1 distances. D) Fourth row shows bivariate distributions of NPC to Lamin B2 distances. First column represents the observed bivariate distribution. Second column represents the expected bivariate distribution. Third column represents the difference between expected and observed. Difference between the observed and expected distance distributions with purple indicating where the observed exceeds the expected frequency and green showing when the observed frequency is less than the expected frequency. Marginal violin plots and box plots of the distances correspond with the half-violin plot counterparts of the same orientation and color as in Panel B of the main figure.

Figure 3–Figure supplement 1. Bivariate histograms of WT MEFs

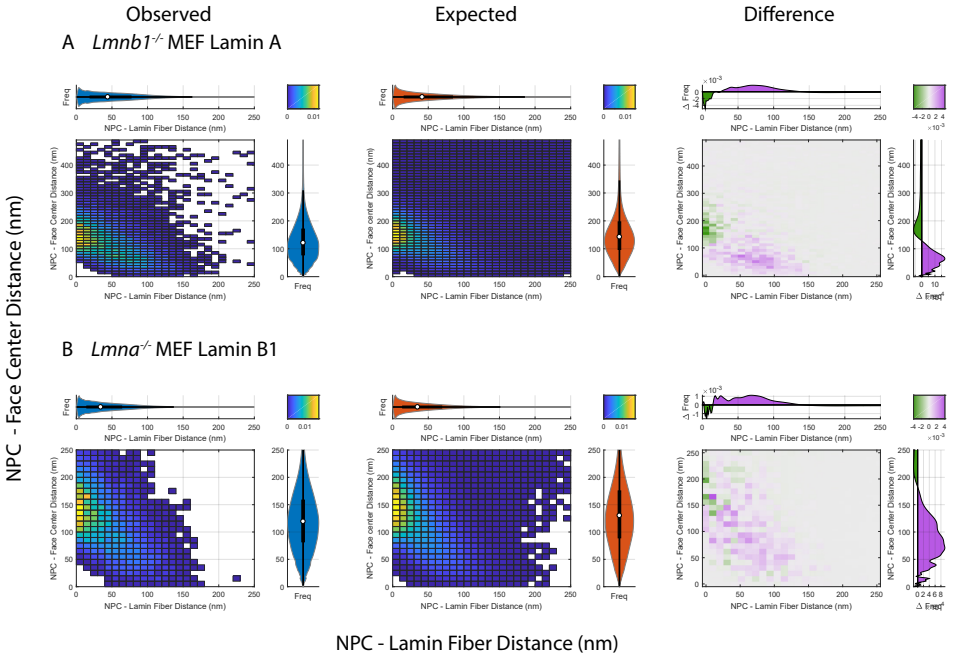

Legend A) First row corresponds NPC to Lamin A fiber and face center distances in *Lmnb1*$^{-/-}$ MEFs. B) Second row shows NPC to Lamin B1 fiber and face center distances in *Lmna*$^{-/-}$ MEFs. Columns are as in Figure 3 – Figure Supplement 1.

Figure 3–Figure supplement 2. Bivariate histograms of *Lmnb1*$^{-/-}$ and *Lmna*$^{-/-}$ MEFs

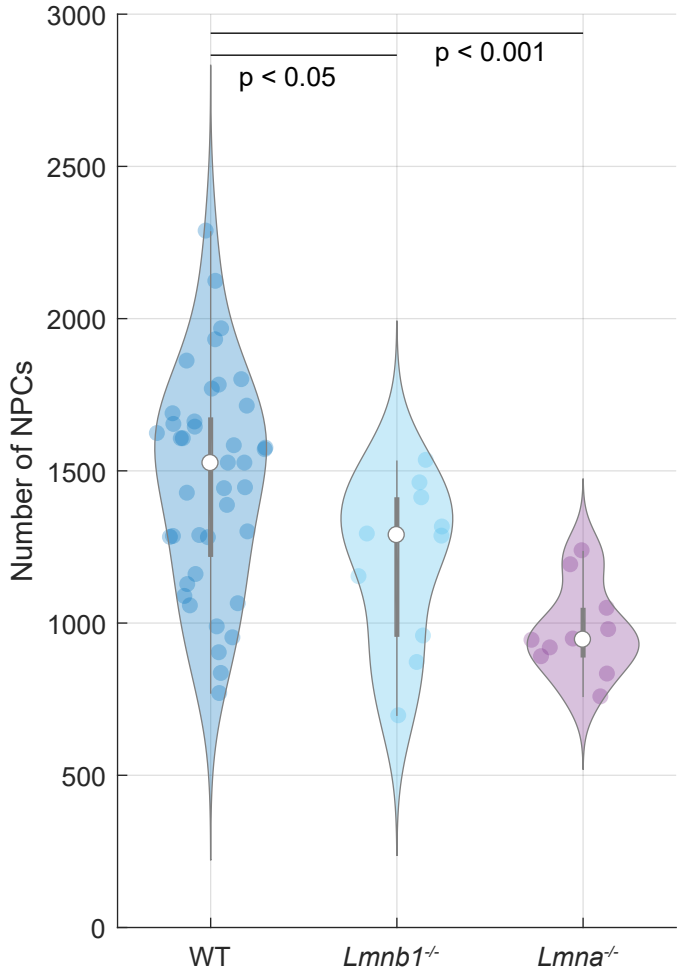

Figure 3–Figure supplement 3. Violin plots comparing the number of NPCs detected in WT *Lmna*$^{-/-}$ and *Lmnb1*$^{-/-}$ MEFs

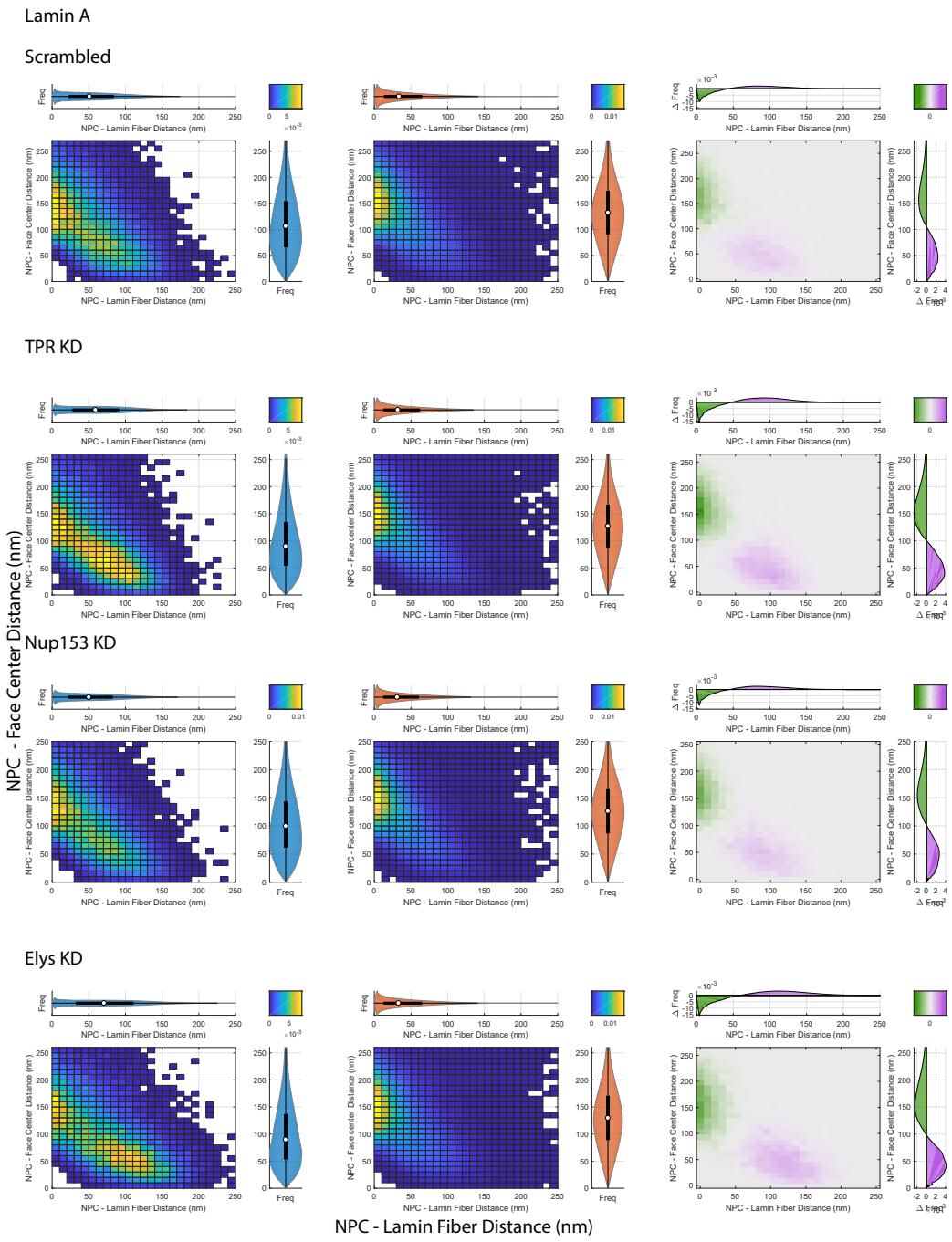

Legend A) First row shows a bivariate distribution of NPC to Lamin A fiber and face center distances in WT MEFs after scramble siRNA. B) Second row shows the same with siRNA knockdown of TPR. C) Third row shows the same with siRNA knockdown of Nup153. D) Fourth row shows the same with siRNA knockdown of Elys. First column represents the observed bivariate distribution. Second column represents the expected bivariate distribution. Third column represents the difference between expected and observed. Difference between the observed and expected distance distributions with purple indicating where the observed exceeds the expected frequency and green showing when the observed frequency is less than the expected frequency. Marginal violin plots and box plots of the distances correspond with the half-violin plot counterparts of the same orientation and color as in Panels B-E of the main figure.

Figure 5–Figure supplement 1. Bivariate histograms of LA Fiber-NPC and Face Center-NPC Distances

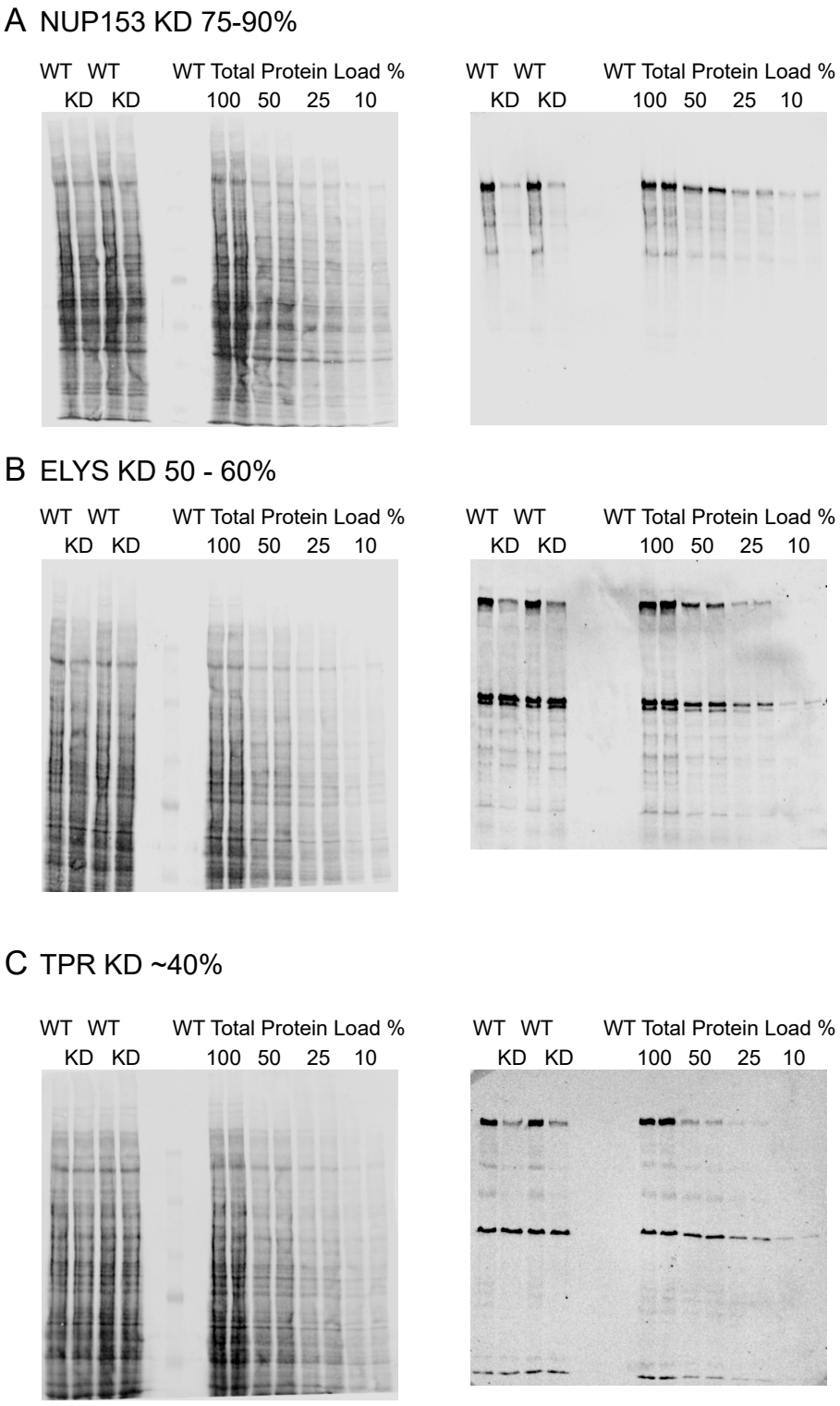

811

Legend siRNA knockdowns were carried out and quantified as described in Materials and Methods. The panels on the left are the total protein stains of the immunoblots with each sample loaded in duplicate. The panels on the right are the immunoblots for each antibody A) NUP153, B) ELYS, C) TPR. The degree of knockdown for each protein was determined by quantifying the average intensity of each duplicate after correction for protein load and comparison to the dilution series of the total protein load from WT cells.

Figure 5–Figure supplement 2. Western Blots of ELYS, NUP153, AND TPR siRNA Knockdown Experiments

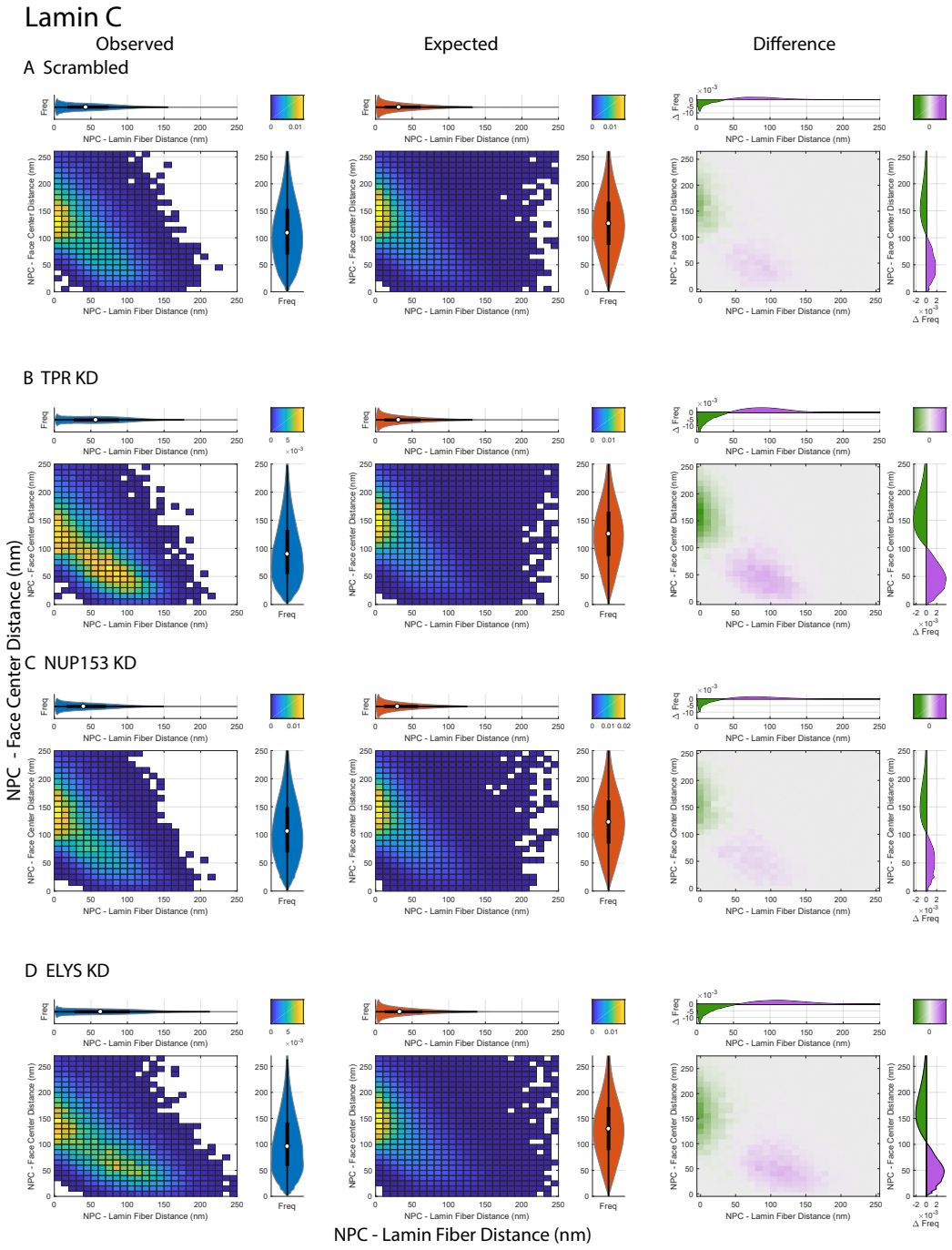

Legend A) First row shows a bivariate distribution of NPC to Lamin C fiber and face center distances in WT MEFs after siRNA knockdown with scramble siRNA. B) Second row shows the same with siRNA knockdown of TPR. C) Third row shows the same with siRNA knockdown of Nup153. D) Fourth row shows the same with siRNA knockdown of Elys. First column represents the observed bivariate distribution. Second column represents the expected bivariate distribution. Third column represents the difference between expected and observed. Difference between the observed and expected distance distributions with purple indicating where the observed exceeds the expected frequency and green showing when the observed frequency is less than the expected frequency. Marginal violin plots and box plots of the distances correspond with the half-violin plot counterparts of the same orientation and color as in Panels B-E of the main figure.

Figure 6–Figure supplement 1. Bivariate histograms of LC Fiber-NPC and Face Center-NPC Distances

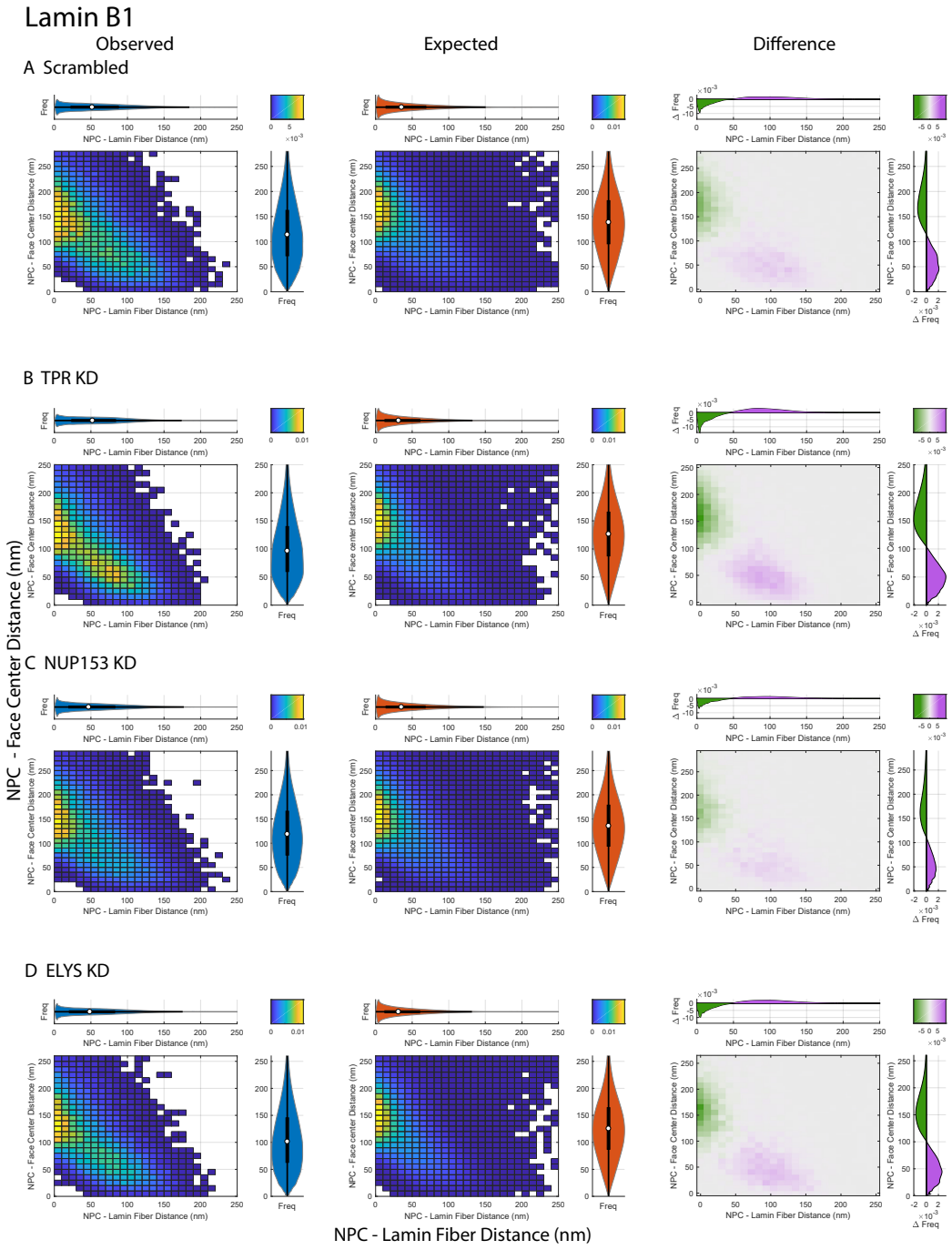

Legend A) First row shows a bivariate distribution of NPC to Lamin B1 fiber and face center distances in WT MEFs after siRNA knockdown with scramble siRNA. B) Second row shows the same with siRNA knockdown of TPR. C) Third row shows the same with siRNA knockdown of Nup153. D) Fourth row shows the same with siRNA knockdown of Elys. First column represents the observed bivariate distribution. Second column represents the expected bivariate distribution. Third column represents the difference between expected and observed. Difference between the observed and expected distance distributions with purple indicating where the observed exceeds the expected frequency and green showing when the observed frequency is less than the expected frequency. Marginal violin plots and box plots of the distances correspond with the half-violin plot counterparts of the same orientation and color as in Panels B-E of the main figure.

Figure 7–Figure supplement 1. Bivariate histograms of LB1 Fiber-NPC and Face Center-NPC Distances

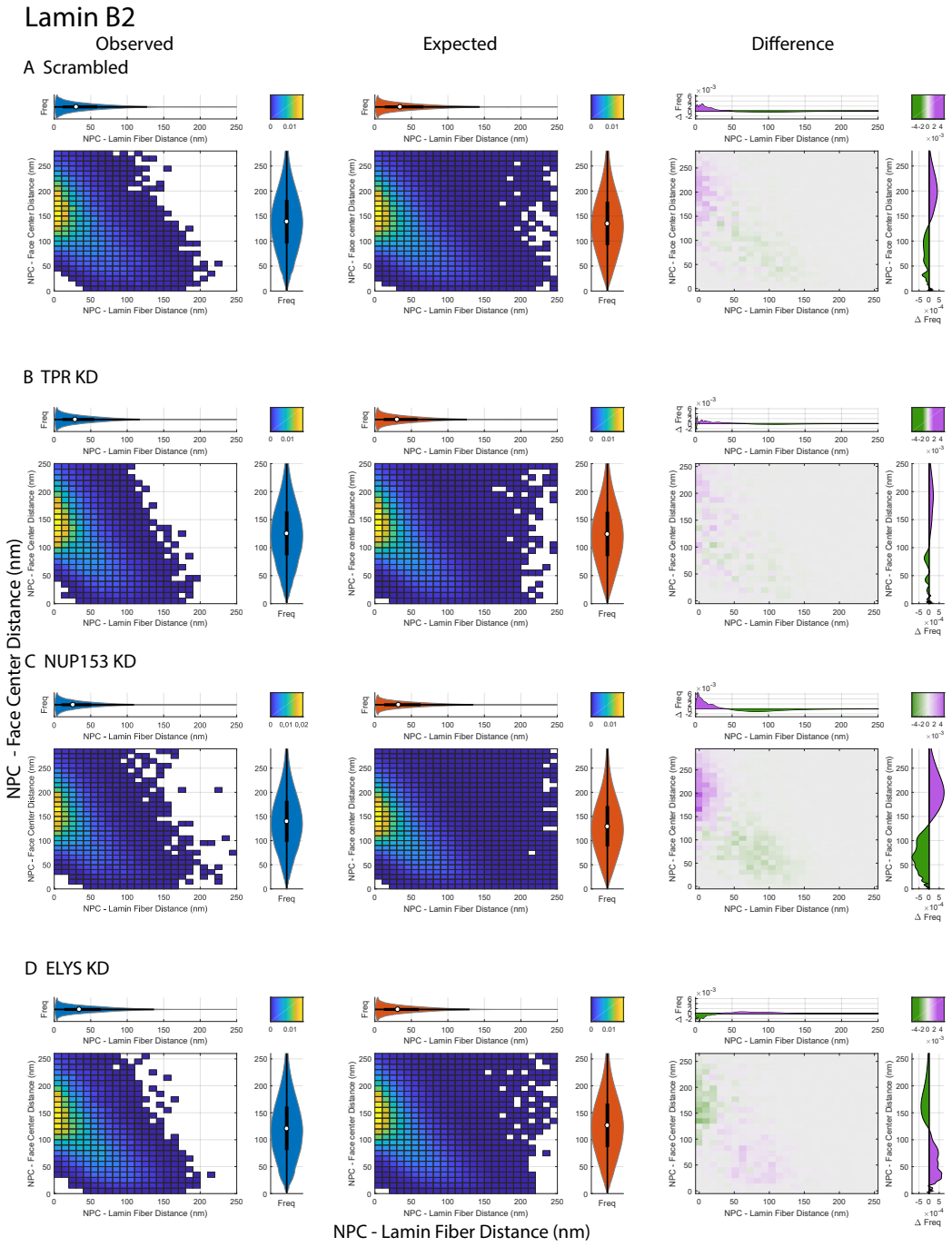

Legend A) First row shows a bivariate distribution of NPC to Lamin B2 fiber and face center distances in WT MEFs after siRNA knockdown with scramble siRNA. B) Second row shows the same with siRNA knockdown of TPR. C) Third row shows the same with siRNA knockdown of Nup153. D) Fourth row shows the same with siRNA knockdown of Elys. First column represents the observed bivariate distribution. Second column represents the expected bivariate distribution. Third column represents the difference between expected and observed. Difference between the observed and expected distance distributions with purple indicating where the observed exceeds the expected frequency and green showing when the observed frequency is less than the expected frequency. Marginal violin plots and box plots of the distances correspond with the half-violin plot counterparts of the same orientation and color as in Panels B-E of the main figure.

Figure 8–Figure supplement 1. Bivariate histograms of LB2 Fiber-NPC and Face Center-NPC Distances

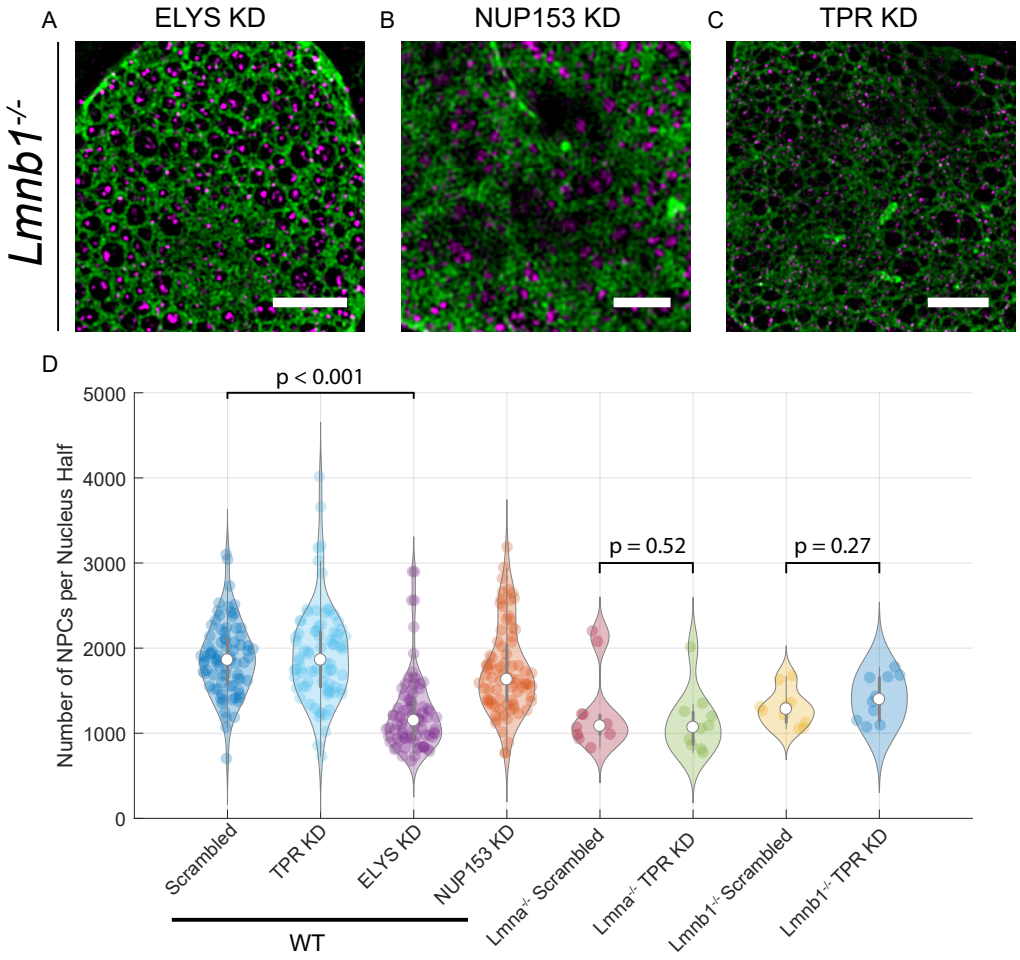

Legend A-C) *Lmnb1*$^{-/-}$ MEFs A) ELYS knockdown, B) NUP153 knockdown, C) TPR knockdown, D) Number of NPCs per half MEF nuclei in a single focal plane in WT MEFs after ELYS, NUP153, and TPR knockdown. Scale Bar = 10 μm

Figure 8–Figure supplement 2. Effect of ELYS, NUP153, and TPR KD in *Lmnb1*$^{-/-}$ and *Lmna*$^{-/-}$ MEFs